nature portfolio

https://doi.org/10.1038/s41586-023-06150-0

Supplementary information

Spin state and deep interior structure of Mars from InSight radio tracking

In the format provided by the authors and unedited

Supplementary Information for

Spin state and deep interior structure of Mars from InSight radio tracking

Authors: Sébastien Le Maistre[1,2*], Attilio Rivoldini[1], Alfonso Caldiero[1,2], Marie Yseboodt[1], Rose-Marie Baland[1], Mikael Beuthe[1], Tim Van Hoolst[1,3], Véronique Dehant[1,2], William M. Folkner[4], Dustin Buccino[4], Daniel Kahan[4], Jean-Charles Marty[5], Daniele Antonangeli[6], James Badro[7], Mélanie Drilleau[8], Alex Konopliv[4], Marie-Julie Péters[1], Ana-Catalina Plesa[9], Henri Samuel[7], Nicola Tosi[9], Mark Wieczorek[10], Philippe Lognonné[7], Mark Panning[4], Suzanne Smrekar[4], W. Bruce Banerdt[4].

Supplementary Discussion

Section 1. GINS-MONTE cross-validation

When using consistent a priori settings, the components of the rotation matrices of MONTE and GINS, positioning the axes of the Mars body-fixed frame, differ by 10^{-9}. This corresponds to a rotation of about 0.5 mas (milliarcseconds) in an angle-axis representation. MONTE, contrary to GINS, is not able in its present state to include the nutation terms induced by Phobos and Deimos (10 and 4 mas amplitude[11]) in the rotation model. Therefore the rotation matrices comparison between both software has been performed without these nutation terms, which are taken into account for the inversion of RISE data with GINS*.

The relative difference in partial derivatives computed by each software is below ~0.5% for both the F factor and FCN frequency. The difference in theoretical Doppler measurements computed by GINS and MONTE with consistent settings is of the order of 0.1 mHz, 10 times smaller than the noise and significantly smaller than the signature of the liquid core (~0.4mHz, Extended Data Figure 1e).

Section 2. A priori value of FCN period

The FCN period parameter, τ_{FCN}, appears in a nonlinear way in the equations (see Eq.2 main paper). This makes the Doppler derivative dependent on the a priori value of τ_{FCN}, which therefore influences the solution. To circumvent the possible hazard of having our τ_{FCN} estimate falling into a local minimum, we adopted an iterative approach where the partial derivative of the Martian rotation and Orientation Parameters (MOPs), and especially those of τ_{FCN}, are computed at each iteration using the numerical values estimated in the previous iteration. Several runs are carried out, each time starting from a different a priori value of τ_{FCN} for iteration 1 taken every 5 days within the range of -275 days to -205 days. Such a range is expected to cover all possible FCN periods for Mars as predicted by interior models[e.g.2,43].

Supplementary Figure S1 clearly shows that when the a priori value of the FCN period is smaller than the ter-annual period (-229 days), the fitted core amplification factor and FCN period converge, while for an FCN a priori value larger than the ter-annual period, there is no convergence.

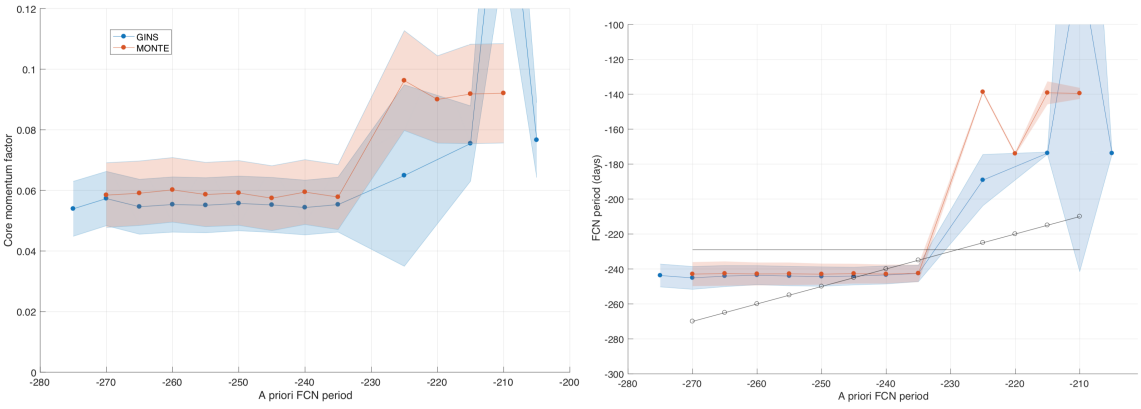

Supplementary Figure S1: Estimated core amplification factor (left) and FCN period (right) as a function of the a priori value of the FCN period, for GINS and MONTE, using 24-months of RISE data (Prime mission). The horizontal line in the graph on the right panel corresponds to the ter-annual period where there can be a resonance. The equation of the black dotted line on the right panel is y=x. It corresponds to the starting a priori value of τ_{FCN}. Shaded envelopes are 1σ uncertainty bounds.

* Note that nutations induced by Phobos and Deimos have negligible impact on the FCN estimate.

Section 3. Inner core signature

For the present-day thermal state of Mars, the iron alloy of the core can only crystallize and form an inner core if the sulfur weight fraction is below 3wt%. Mass conservation then implies that the core radius must be smaller than about 1400 km, which is not in agreement with the core amplification factor F determined in this study and with estimates deduced from tides[18] and from core reflected shear waves[17]. Interior structure models that agree with the findings of this study require a large fraction of light elements (see Fig. 4 of the main paper) and consequently the core temperature must be significantly below any plausible present-day estimate for an inner core to be possible (Supp: Core structure and composition). The transfer function we use in the main paper (see Eq.2) therefore applies to the case of a fully liquid core and is expressed in terms of a resonance with the Free Core Nutation. If, despite what just preceded, Mars has a solid inner core, the transfer function would depend on an additional nutational normal mode, the Free Inner Core Nutation (FICN)[3]. Similarly to the FCN mode, which represents a relative motion of the liquid (part of the) core with respect to the mantle, the FICN describes a relative rotation of the inner core with respect to the outer core and mantle. Contrary to the FCN, which results in a retrograde motion of the rotation axis in space (ω_{FCN}<0), the FICN (also referred to as the Prograde Free Core Nutation or PFCN) has a prograde frequency (ω_{FICN} >0). We here show that the inclusion of an inner core in the transfer function does not significantly affect the estimation of the F factor and the FCN period and that the resonance strength of the FICN resonance is consistent with zero.

The transfer function that takes into account an inner core can be expressed as

$$T_F(\omega) = 1 + F\frac{\omega}{\omega - \omega_{FCN}} + F^\star\frac{\omega}{\omega - \omega_{FICN}}, \qquad (S1)$$

where ω_{FICN} is the unknown FICN prograde frequency, and $F^\star$ the FICN resonance strength. A preliminary analysis with transfer function (Eq.$(S1)$) did not allow us to reliably estimate the four transfer function parameters simultaneously. This is mainly because the $\tau_{FICN} = 2\pi/\omega_{FICN}$ estimate is strongly driven by its a priori value and never properly converges, whatever the a priori value taken between 200 and 575 days[30]. Therefore, we only fitted ω_{FCN}, F and $F^\star$ along with the other MOPs and position parameters, for a range of chosen values for ω_{FICN}. We get $F = 0.052 \pm 0.022$ (see solid orange curve in Supplementary Figure S2) and $\tau_{FCN} = -242.5 \pm 11$ days. Both values are within the 1σ intervals of the results for an entirely liquid core (see Supplementary Table S1 and Extended Data Table 2), but affected by error bars ~4 times larger. The results for F and τ_{FCN} are therefore not significantly affected by the simultaneous estimation of $F^\star$ and the value set for ω_{FICN}. Our $F^\star$ estimate is always consistent with zero at 1σ and the average solution is $\bar{F}^\star = 4.10^{-5} \pm 0.007$. Supplementary Figure S2 dashed curves show the temporal evolution of our $F^\star$ estimate for different scenarios of fit (see details in the caption of the figure). The uncertainty bound of $F^\star$ in the joint estimation case has been calibrated to account for the variability of the solutions as a function of the FICN period. We conclude from this analysis that $F^\star \simeq 0$, indicating that no signature of an inner core is observed in the data and that the use of Eq.2 (main paper) for T_F is justified.

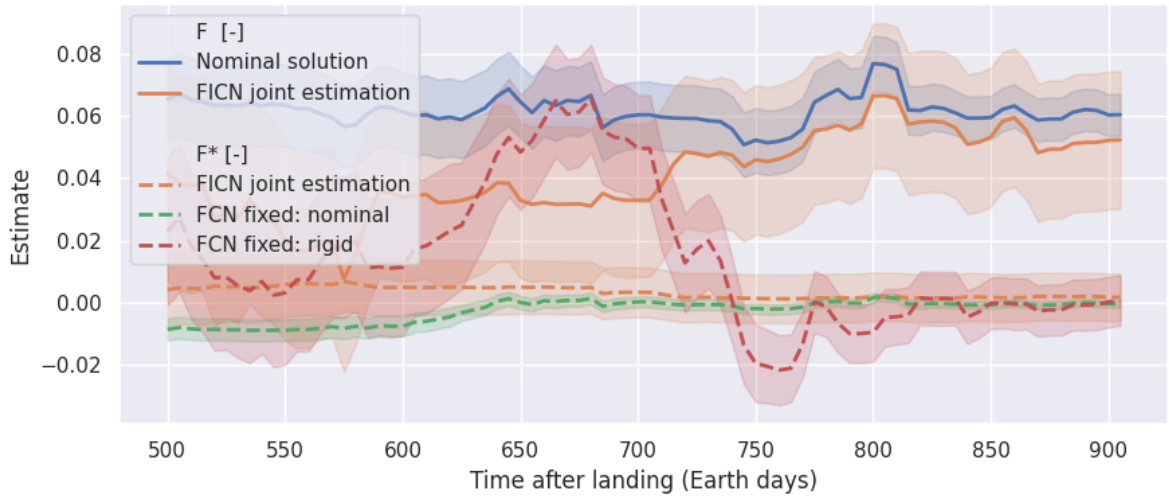

Supplementary Figure S2: Temporal evolution of preliminary estimates of $F^\star$ (dashed curves) assuming no FCN contribution (i.e. $F = 0$ in Eq.$(S1)$) for the "rigid" case or assuming $F = 0.06$ and $\tau_{FCN} = -243$ days for the "nominal" case. Orange solutions are obtained from a joint estimation of τ_{FCN}, F (solid curve) and $F^\star$ (dashed curve) and with $\tau_{FICN} = 400$ days. Shaded envelopes are 1σ uncertainties expect for $F^\star$ uncertainty which is up-scaled to a conservative value $\sigma_{\bar{F}^\star} = 0.007$ that takes into account our lack of knowledge on τ_{FICN}. The nutation transfer function parameters are always fitted along with the full set of MOPs.

Section 4. Full set of estimated parameters

Our solutions using the 24-months Prime mission data and the full set of 30-months of data that have been pre-processed so far are reported in Supplementary Table S1, along with the a priori values of the parameters and the constraints. They have been obtained using GINS and MONTE independently.
The Prime mission solutions are obtained with the classical rotation model, while the Full-arc solutions require the post-dust-storm model to stabilize the solutions (see Methods and Extended Data Figure 1d). Note that the quadratic terms added in the longitude and obliquity angles of the post-dust-storm model does not really help improving the solution stability. We expected the deficiency in the rotation model to come from the spin angle, for which variations are hard to predict: atmospheric phenomena (e.g. dust storms) can excite planet rotation variations in a broad frequency band, whereas the nutation frequencies are known from celestial mechanics. Therefore, we extensively tested improvements to the modelling of the spin angle that would help stabilize the solution. An extension of the spin series to harmonics up to order eight and the addition of a bi-annual term did not improve our estimates. The spin angle amplitudes at harmonics higher than order four were consistent with zero, meaning that order four is still adequate for RISE. We obtained a significant improvement in the stabilization of the nutation solution by fitting separately the first ~150 days of data and the remaining data as explained in Methods. As an alternative approach to the modeling of the slope in the residuals, we fitted two other extra parameters for the first 150d interval: a bias in the initial spin angle ($\delta\phi_0$) and one in the rotation rate ($\delta\dot{\phi}$). The latter is a correction to the global estimate of $\dot{\phi}$, itself obtained from the entire set of RISE and Viking combined. The corresponding MOP solution, not shown here, is consistent with that of the post-dust-storm model. Moreover, the estimates of $\delta\phi_0 \approx 6.3\ 10^{-6} \pm 7.7\ 10^{-7}$ deg and $\delta\dot{\phi} \approx -6.3\ 10^{-8} \pm 6.5\ 10^{-9}$ deg/day support the hypothesis of a deceleration of the planet in the early phase of the mission.

Full arc solutions are used to provide the preferred solutions, reported in Extended Data Table 2, which basically consists of the average of the GINS and MONTE sets of full arc solutions ($p = (p_M + p_G)/2$), with error bars computed as follows $\sigma = \sqrt{\frac{{\sigma_M}^2 + {\sigma_G}^2 + (p_M - p_G)^2}{2}}$, where $p_M \pm \sigma_M$ and $p_G \pm \sigma_G$ are MONTE and GINS solutions (central value plus or minus formal errors), respectively. Note that the corresponding lander positions and spin amplitudes at Viking era can also be retrieved by averaging GINS and MONTE full arc solutions.

The last column of Supplementary Table S1 provides the overlapping factor $\kappa = |p_M - p_G|/\sqrt{(\sigma_M^2 + \sigma_G^2)}$, by which the MONTE and GINS full-arc uncertainties need to be multiplied in order to overlap. Note that our geophysical interpretations and conclusions, based on our preferred solution of Extended Data Table 2, take full account of these GINS-MONTE differences. Note also that the overlapping factors are systematically lower than one when comparing our solutions with those of Folkner et al. (1997)[5], meaning that our solutions are compliant at one sigma with the latter. It is worth mentioning that Folkner et al. (1997)[5] fitted the MOP to the combined Viking and Mars Pathfinder data, but the very short Pathfinder life time (90 days) has a very small influence on the spin series amplitude estimates, which involve periods greater than 171 days (quarter-annual). Also worth mentioning is that both MONTE and GINS solutions have at least one large amplitude estimate (i.e. above 20 mas) for either the ter- or the quarter-annual wave or for both, which is difficult to explain/believe.
The difference between GINS and MONTE in the estimates of the equatorial coordinates of the lander's antennas (X and Y) is mainly due to the difference in the $\ddot{\phi}$ estimates and to the shift in ϕ_0 for the GINS solutions, which is inherent in the conversion from α, δ, W to I, ψ, ϕ[61].
Supplementary Figure S3 shows the compatibility of the Full-arc solutions of Supplementary Table S1 with the nominal solution of this paper (as reported in Extended Data Table 2) and with three recent solutions from the literature[10,62,48].

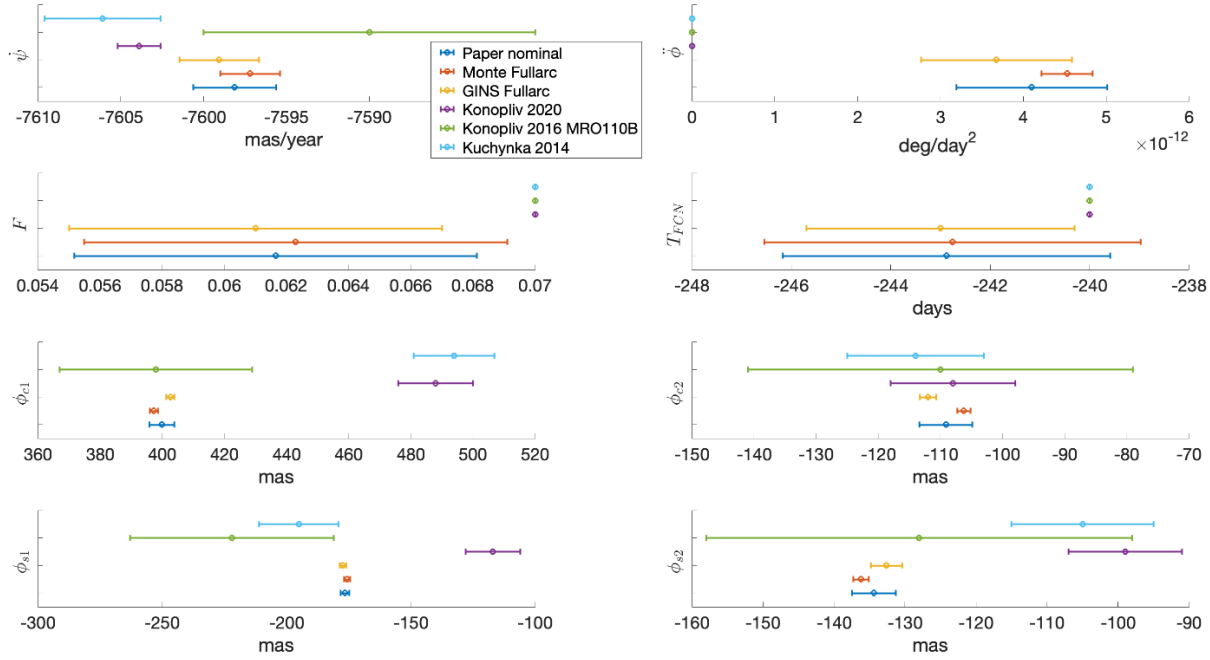

Supplementary Figure S3: Compatibility of our Full-arc solutions with recently published solutions[10,62,48]. Error bars are 1σ uncertainties.

Parameter	Symbol	Unit	A priori value	A priori const	Value and Uncertainty				Overlapping factor between GINS and MONTE Full-arc
					GINS		MONTE		
					Prime mission (1st dataset of 735d)	**Full-arc** (of 905 days)	**Prime mission** (1st dataset of 735d)	**Full-arc** (of 905 days)	
Mars orbit inclination of 1980	J	deg	24.67682669	-	fixed	fixed	fixed	fixed	-
Longitude of Mars orbit ascending node of 1980	N	deg	3.37919183	-	fixed	fixed	fixed	fixed	-
Prime meridian at J2000 wrt Mars orbit at 1980	ϕ_0	deg	133.386373	-	133.38641351* ± 0.000012	133.38641504* ± 0.0000074	fixed	fixed	-
Longitude of node at J2000 wrt Mars orbit at 1980	ψ_0	deg	81.968392	0.0028	81.96836305 ± 0.000011	81.96836478 ± 0.0000104	81.96836513 ± 0.00001	81.96835322 ± 0.0000100	0.80
Precession rate at J2000 wrt Mars orbit at 1980	$\dot{\psi}$	mas/yr	-7603.9	100	-7598.235 ± 2.4	-7599.057 ± 2.4	-7599.170 ± 1.9	-7597.195 ± 1.80	0.62
Quadratic longitude coefficient	$\ddot{\psi}$	mas/yr^2	-0.0144	-	fixed	fixed	fixed	fixed	-
Obliquity at J2000 wrt Mars orbit at 1980	I_0	deg	25.189381	0.0028	25.18940990 ± 0.0000052	25.18941255 ± 0.0000047	25.18940909 ± 0.0000045	25.18940603 ± 0.0000044	1.00
Obliquity rate at J2000 wrt Mars orbit at 1980	$\dot{I}$	mas/yr	-1.2	100	-8.129 ± 1	-8.682 ± 1	-8.080 ± 0.80	-7.301 ± 0.79	1.08
Quadratic obliquity	$\ddot{I}$	mas/yr^2	0.0020	-	fixed	fixed	fixed	fixed	-

coefficient										
Rotation rate at J2000 wrt Mars orbit at 1980		$\dot{\phi}$	deg/day	350.891985314	-	350.891985349438 ± 0.000000013	350.891985346409 ± 0.000000014	350.891985325764 ± 0.0000000050	350.891985331763 ± 0.0000000049	0.99
Rotation quadratic coefficient		$\ddot{\phi}$	deg/day^2	0	2e-10	2.6078e-12 ± 8.9e-13	3.7017e-12 ± 9.1e-13	3.9741e-12 ± 3.1e-13	4.5291e-12 ± 3.1e-13	0.86
Core amplification factor		F	-	0.07	-	0.057 ± 0.009	0.061 ± 0.006	0.060 ± 0.011	0.062 ± 0.0068	0.14
FCN period		τ_{FCN}	day	-240	-	-243.9 ± 5.1	-243.0 ± 2.7	-243.1 ± 5.5	-242.8 ± 3.8	0.05
LOD variation amplitudes	Viking era	ϕ_{C1}	mas	488	100	549 ± 14	546 ± 15	525 ± 6	526 ± 6	1.26
		ϕ_{C2}	mas	-108	100	-65 ± 24	-71 ± 25	-112 ± 8	-108 ± 8	1.41
		ϕ_{C3}	mas	-16	100	9 ± 21	-1 ± 21	-41 ± 9	-36 ± 9	1.56
		ϕ_{C4}	mas	3	100	-51 ± 19	-42 ± 19	-34 ± 7	-34 ± 7	0.38
		ϕ_{S1}	mas	-117	100	-179 ± 28	-175 ± 28	-206 ± 11	-219 ± 11	1.48
		ϕ_{S2}	mas	-99	100	-29 ± 20	-35 ± 20	-69 ± 9	-74 ± 8	1.80
		ϕ_{S3}	mas	-9	100	-17 ± 24	-5 ± 24	28 ± 10	22 ± 10	1.04
		ϕ_{S4}	mas	-2	100	-21 ± 19	-18 ± 20	-3 ± 7	-5 ± 6	0.61
	InSight era	ϕ_{C1}	mas	488	100	414.2 ± 1.5	402.6 ± 1.3	415.0 ± 1.6	397.3 ± 1.3	2.89
		ϕ_{C2}	mas	-108	100	-111.5 ± 1.5	-112.0 ± 1.3	-109.3 ± 1.3	-106.2 ± 1.1	3.44
		ϕ_{C3}	mas	-16	100	-9.0 ± 1.2	-10.7 ± 0.8	-9.3 ± 1.0	-8.8 ± 0.8	1.69
		ϕ_{C4}	mas	3	100	-4.4 ± 0.9	-1.0 ± 0.7	-3.8 ± 1.0	1.7 ± 0.9	2.42
		ϕ_{S1}	mas	-117	100	-182.7 ± 1.7	-177.3 ± 1.3	-181.6 ± 1.3	-175.6 ± 1.2	0.93
		ϕ_{S2}	mas	-99	100	-128.8 ± 3.3	-132.6 ± 2.2	-132.1 ± 1.2	-136.2 ± 1.1	1.46

		ϕ_{S3}	mas	-9	100	-17.7 ± 1.8	-20.8 ± 1.4	-19.1 ± 0.7	-23.7 ± 0.6	1.88
		ϕ_{S4}	mas	-2	100	-11.0 ± 0.9	-11.9 ± 0.7	-12.1 ± 0.9	-11.5 ± 0.7	0.37
Dust parameter		$\delta\phi_{c1}$	mas	0	100	-	37 ± 4.9	-	28 ± 3	1.57
		$\delta\phi_{s1}$	mas	0	100	-	-20 ± 7.3	-	0.2 ± 2	2.67
Insight West antenna coordinates (body-fixed frame)		x_w	m	-2417532.54	1000	-2417505.9 ± 2	-2417504.5 ± 2	-2417511.8 ± 0.9	-2417508.9 ± 0.9	2.01
		y_w	m	2365926.6	1000	2365953.1 ± 2	2365954.5 ± 2	2365947.0 ± 0.9	2365950.0 ± 0.9	2.05
		z_w	m	266330.0	20	266248.9 ± 17	266266.7 ± 16	266307.3 ± 15	266338.3 ± 13.8	3.39
Insight East antenna coordinates (body-fixed frame)		x_e	m	-2417533.60	1000	-2417507.0 ± 2	-2417505.5 ± 2	-2417512.9 ± 0.9	-2417510.0 ± 0.9	2.05
		y_e	m	2365925.8	1000	2365952.2 ± 2	2365953.8 ± 2	2365946.2 ± 0.9	2365949.2 ± 0.9	2.10
		z_e	m	266330.0	20	266248.7 ± 17	266266.3 ± 16	266307.3 ± 15	266336.7 ± 14	3.31
Viking L1 antenna coordinates (body-fixed frame)		x_v	m	2100790.03	1000	2100724 ± 6	2100719 ± 7	2100714 ± 2	2100716 ± 2	0.41
		y_v	m	-2329042.25	1000	-2329101 ± 6	-2329105 ± 6	-2329110 ± 2	-2329109 ± 2	0.63
		z_v	m	1284466.76	20	1284397 ± 84	1284396 ± 88	1284436 ± 20	1284381 ± 20	0.17

Supplementary Table S1: Parameters estimates obtained using the first 24 months (~735d) of RISE data (Prime mission results) and the full set of 30 months of data (full arc results), systematically combined with the Viking 1 lander data. Uncertainties are 1σ formal errors. *Because GINS works in α, δ, W, the angle W_0 is fixed but ϕ_0 varies from one solution to another due to the difference in the α_0 and δ_0 estimates. Despite their level of uncertainty (i.e. significant digits), angles (º), rates (mas/yr and º/d) and quadratic (º/d^2) estimates are given with 8, 3, 12 and 16 digits respectively in order to ensure 0.1 mas precision in the angles conversion between (α, δ, W) and (ψ, I, ϕ), even when computed 20 years away from J2000[61].

The matrix of correlations of the main parameters is shown in Extended Data Figure 3b and the full correlation matrix provided as csv file (Source Data). From this figure, we see that F and the FCN period are significantly correlated with each other and with the spin angle amplitudes, especially F and ϕ_{s2}. Despite the long data span of Viking plus RISE combination, and the high accuracy of RISE data, we still observe high (anti) correlations between ψ_0 and $\dot{\psi}$ and between I_0 and $\dot{I}$. These correlations are primarily responsible for the difference in precession rate with respect to our result based on one Earth year only[44], which was obtained with stronger a priori constraints on the angles at J2000 (ψ_0,I_0). They also explain the difference with the orbiter estimate[10] that we retrieve exactly by fixing (ψ_0,I_0) to Konopliv et al. (2020)[10], with no significant impact on the nutation estimates. Moreover, the significant change in our $\dot{\phi}$ estimate with respect to Kahan et al. (2021)[44] indirectly affects the precession estimate since correlations between $\dot{\phi}$ and $\dot{\psi}$ are rather strong. This change of $\dot{\phi}$ of more than two times its error bars results from the estimation of a new parameter, $\ddot{\phi}$, which allowed us to model the accelerating rotation observed between Viking and RISE eras.

Following previous studies (see e.g. Fig. 18 of Konopliv et al. (2006)[42]), we chose to describe the orientation of Mars with respect to the mean orbit of Mars of 1980 (see Supplementary Table S1). Considering Mars mean orbit of epoch J2000 instead, we would have $N = 3°.37321423$ and $J = 24°.67706841$ for the angles orienting the mean orbit with respect to ICRF. The prior values for Mars orientation angles would be $\phi_0 = 133°.384992$ ($\dot{\phi} = 350.891985313422\,°/day$), $I_0 = 25°.191818$ ($\dot{I} = -1.28\,mas/yr$), and $\psi_0 = 81°.975074$ ($\dot{\psi} = -7603.21\,mas/yr$). For the preferred solution: $\phi_0 = 133°.3850127$ ($\dot{\phi} = 350.891985338504\,°/day$), $I_0 = 25°.19184671$ ($\dot{I} = -7.98\,mas/yr$), and $\psi_0 = 81°.97504061$ ($\dot{\psi} = -7597.41\,mas/yr$).

As specified before, the GINS software works with α, δ, W angles, which are converted in I, ψ, ϕ in a post-processing phase of the analysis. The angles at epoch, rates, and periodic variations are converted using the geometrical relations between the two sets of angles that can be derived by equating Eqs. (4) and (5) (of the Methods). Specifically, those relations take the following analytical form for the periodic variations in angles orienting the spin axis in space:

$$\Delta\psi = \Delta\alpha\,\frac{cos\,J - sin\delta cos I_0}{sin^2 I_0} + \Delta\delta\,\frac{\sin J\cos(\alpha_0 - N)}{sin^2 I_0}, \qquad (S2)$$

$$\Delta I = \Delta\alpha\,\frac{cos\,\delta_0 \sin\,J\cos\,(\alpha_0 - N)}{sin\,I_0} - \Delta\delta\,\frac{\cos\delta_0\cos J + \sin\delta_0\sin J\sin(\alpha_0 - N)}{sin\,I_0}. \qquad (S3)$$

Replacing the non-Δ quantities of the above equation by their numerical values, we get

$$\Delta\psi = 1.03258\,\Delta\alpha\; + 1.60964\,\Delta\delta, \qquad (S4)$$

$$\Delta I = 0.41341\,\Delta\alpha\; - 0.72841\,\Delta\delta. \qquad (S5)$$

The spin angle amplitudes are modeled in GINS according to the following formalism

$$\Delta W = \sum_{j=1}^{4}\left(W_{cj}\cos(jnt)\; + W_{sj}\sin(jnt)\right), \qquad (S6)$$

where n is the mean motion of Mars and t is the time past J2000. Reminding that $M = n\,t\; +\; M_0$, with the Mars mean anomaly at J2000 $M_0 =\; 19.35743065°$, the above W_{cj}, W_{sj} amplitudes for the spin angle can be converted into ϕ_{cj}, ϕ_{sj} amplitudes of Eq.(6) (see Methods) according to:

$$\phi_{cj} = \left(W_{cj} + \alpha_{cj}\,sin\delta_0\right)cos(jM_0) - \left(W_{sj} + \alpha_{sj}\,sin\delta_0\right)sin(jM_0), \qquad (S7)$$

$$\phi_{sj} = \left(W_{sj} + \alpha_{sj}\,sin\delta_0\right)cos(jM_0) + \left(W_{cj} + \alpha_{cj}\,sin\delta_0\right)sin(jM_0) - \phi_{rj}, \qquad (S8)$$

ϕ_{rj} are the relativistic periodic corrections due to variations in Mars orbit radius[6,42] that we apply to our raw amplitude estimates to produce our ϕ_{cj}, ϕ_{sj} solutions reported in Supplementary Table S1. We use $\phi_{r1} = -166.95\,mas, \phi_{r2} = -7.78\,mas$ and $, \phi_{r3} = -0.54\,mas$[45]. The α_{cj},α_{sj} amplitudes are the amplitudes of nutation computed from the rigid nutation (α^r_{cj},α^r_{sj}, δ^r_{cj},δ^r_{sj}) of Baland et al. (2020)[11] (see https://doi.org/10.24414/h5pn-7n71, last columns of bottom table at https://lara.oma.be/RigidNutations/bman20rs.dat) according to:

$$\alpha_{cj} = \alpha_{cj}^{r}\left(1 + F\frac{(jn)^2}{(jn)^2 - \omega_{FCN}^2}\right) + \delta_{sj}^{r}cos^{-1}(\delta_0)\left(F\frac{jn\omega_{FCN}}{(jn)^2 - \omega_{FCN}^2}\right), \quad (S9)$$

$$\alpha_{sj} = \alpha_{sj}^{r}\left(1 + F\frac{(jn)^2}{(jn)^2 - \omega_{FCN}^2}\right) - \delta_{cj}^{r}cos^{-1}(\delta_0)\left(F\frac{jn\omega_{FCN}}{(jn)^2 - \omega_{FCN}^2}\right), \quad (S10)$$

$$\delta_{cj} = \delta_{cj}^{r}\left(1 + F\frac{(jn)^2}{(jn)^2 - \omega_{FCN}^2}\right) - \alpha_{sj}^{r}cos(\delta_0)\left(F\frac{jn\omega_{FCN}}{(jn)^2 - \omega_{FCN}^2}\right), \quad (S11)$$

$$\delta_{sj} = \delta_{sj}^{r}\left(1 + F\frac{(jn)^2}{(jn)^2 - \omega_{FCN}^2}\right) + \alpha_{cj}^{r}cos(\delta_0)\left(F\frac{jn\omega_{FCN}}{(jn)^2 - \omega_{FCN}^2}\right). \quad (S12)$$

The GINS raw solutions in α, δ, W, equivalent to the Full-arc solution reported in Supplementary Table S1, are shown in Supplementary Table S2 below.

Parameter		**Symbol**	**Unit**	**GINS**
Right ascension at J2000		α_0	deg	317.681132336 ± 0.0000075
Right ascension rate		$\dot{\alpha}$	mas/yr	-3914.253 ± 1.3
Quadratic right ascension coefficient		$\ddot{\alpha}$	mas/yr^2	-0.0108 (fixed)
Declination at J2000		δ_0	deg	52.88632054 ± 0.0000066
Declination rate		$\dot{\delta}$	mas/yr	-2209.5470 ± 1.2
Quadratic declination coefficient		$\ddot{\delta}$	mas/yr^2	0.0159 (fixed)
Prime meridian at J2000		W_0	deg	176.63198979682688 (fixed)
Rotation rate		$\dot{W}$	deg/day	350.891982490642 ± 0.000000014
Quadratic Rotation coefficient		$\ddot{W}$	deg/day^2	3.6660e-12 ± 9.1e-13
Core amplification factor		F	-	0.061 ± 0.006
FCN period		τ_{FCN}	day	-243.0 ± 2.7
LOD variations amplitudes	Viking era	W_{C1}	mas	463 ± 15
		W_{C2}	mas	413 ± 25
		W_{C3}	mas	134 ± 21
		W_{C4}	mas	0 ± 19
		W_{S1}	mas	-318 ± 28
		W_{S2}	mas	483 ± 20
		W_{S3}	mas	53 ± 24
		W_{S4}	mas	39 ± 20
	InSight era	W_{C1}	mas	327.6 ± 1.3
		W_{C2}	mas	320.3 ± 1.3
		W_{C3}	mas	115.1 ± 0.8

		W_{C4}	mas	13.3 ± 0.7
		W_{S1}	mas	-272.2 ± 1.3
		W_{S2}	mas	432.3 ± 2.2
		W_{S3}	mas	52.3 ± 1.4
		W_{S4}	mas	0.2 ± 0.7
Dust parameters		W_{cd}	mas	26 ± 7.3
		W_{sd}	mas	-27± 4.9

Supplementary Table S2: Estimated parameters using GINS with the post-dust-storm model (full-arc solution). Uncertainties are 1σ formal errors.

Section 5. Principal moments of inertia

Following Baland et al. (2020)[11], the relation between the precession rate of Mars $\dot{\psi}$ and the polar moment of inertia C can be summed up as $C/m_a{r_e}^2 = -1415393\,J_2\,/\,(\dot{\psi}-\dot{\psi}_g)$ where $\dot{\psi}$ and $\dot{\psi}_g$ are expressed in mas/year. $\dot{\psi}_g = 6.754$ mas/year is the geodetic precession. $\dot{\psi}$ is expressed with respect to the Mars mean orbit of epoch J2000. This relation accounts for the external torques exerted by the Sun, Phobos and Deimos, and the other planets, on the oblate shape of Mars. The effects of triaxiality on the precession rate of Mars averages out. Given the precession rate determined in the present study, and the gravity field $J_2 = 0.0019566$ from Konopliv et al. (2020)[10] (MRO120F solution), $C/m_a{r_e}^2 = 0.36419 \pm 0.00011$, where $m_a = 6.41712 \times 10^{23}$ kg for the mass of Mars[10]. The mean moment of inertia is then obtained as $MOI = (C/m_a{r_e}^2 - 2/3\,J_2)({r_e}^2/{r_a}^2) = 0.36428 \pm 0.00011$. $r_e = 3396$ km is the reference radius of the MRO120F solution and $r_a = 3389.5$ km is the mean planetary radius. The principal moments of inertia are $A/m_a{r_a}^2 = 0.363499$, $B/m_a{r_a}^2 = 0.363752$, $C/m_a{r_a}^2 = 0.365589$, with the three of them affected by the same level of uncertainty of 0.00011. Note that there is a typo in Konopliv et al. (2020)[10] for the uncertainty of C, which should be 10 times smaller than the value reported of 0.0006.

Section 6. Equation of state for the liquid core

To model the thermoelastic properties of the liquid core we assume that the liquid Fe-O-S-C-H alloy can be described by an asymmetric Margules mixing model that uses Fe, FeO, FeS, Fe_3C, and FeH as end-members. The volume of the thermodynamic Fe-O-S-C-H solution writes

$$V(p,T) = V_{ideal}(p,T) + V_{ex}(p,T), \qquad (S13)$$

where

$$V_{ideal}(p,T) = \sum_{i=\{Fe,FeO,Fe_3C,FeH\}} \chi_i\, V_i(p,T)$$

and

$$V_{ex}(p,T) = \chi_{Fe}\chi_{FeO}(\chi_{FeO}W_{Fe-FeO} + \chi_{Fe}\,W_{FeO-Fe}) + \chi_{Fe}\chi_{FeS}\big(\chi_{FeS}W_{Fe-FeS}(p,T) + \chi_{Fe}\,W_{FeS-Fe}(p,T)\big). \qquad (S14)$$

The χ_i and $V_i(p,T)$ are the molar fraction and molar volumes of Fe, FeO, FeS, Fe_3C, and FeH, and $\chi_{Fe} = 1 - \chi_{FeO} - \chi_{FeS} - \chi_{Fe_3C} - \chi_{FeH}$. The thermal expansivity and the isothermal bulk modulus of the solution can then be calculated from Eq.$(S13)$ using classical thermodynamic relations. The isobaric heat capacity C_p is computed from the end-members assuming ideality. For the equation of state (EoS) of liquid Fe and liquid FeO we use Dorogokupets et al. (2017)[66] and Komabayashi (2014)[67]. To describe the elastic properties of FeS and Fe_3C we use the Anderson-Grüneisen EoS[e.g.67]. The EoS parameters for both end-members have been obtained by fitting the EoS to a large set of experimental data[68,69,70,71,72,73,74,75,76,109] assuming the thermodynamic model of Xu et al (2021)[68] for Fe-FeS and ideal mixing for Fe-Fe_3C. The EoS parameters for FeS and Fe_3C are given in

Supplementary Table **S3**. The Margules coefficients for Fe-FeO can be obtained by deriving Eq.(10) of Komabayashi (2014)[67] with respect to pressure; those for Fe-FeS are given in
Supplementary Table **S3**. An equation of state for liquid FeH at Mars' core conditions is not available. We therefore use the equation of state describing the volume of interstitial H[65] in solid iron together with an equation of state of fcc Fe[66]. To take into account the volume difference between the solid and liquid phase, we increase the volume of solid FeH by the relative density difference between liquid and fcc (~2.-2.4%).

	T_0 K	V cm^3/mol	C_p $J/K/mol$	α $10^5/K$	K_T GPa	$K_T{}'$	γ	δ_T	W_{Fe-X} cm^3/mol	W_{X-Fe} cm^3/mol	B_0 GPa	B'
FeS	1650	24.4±0.3	62.5	11.8	12.0±-0.8	6.9±0.3	0.62±0.04	0.4±0.5	-9.9±1.4	-3.54±0.4	3.02±0.3	2.6±0.4
Fe_3C	1723	26.5±0.1	215.	14.8±5.	57.5±13	15.±3.	1.34±0.4	9.1±4.0	-	-	-	-

Supplementary Table S3: Equation of state parameters for liquid solution end-members and Margules coefficients. For both $\kappa = 1.4$ and X stands for FeS or Fe_3C.

Section 7. Thermal state of the mantle

We compute the thermal evolution in a 3D spherical geometry to determine the spatial and temporal evolution of mantle flow throughout Mars' thermal history. In our approach we employ a 3D crust whose thickness variations is derived from gravity and topography data[20,64]. The temperature distribution in the interior of Mars at present day is the result of 4.5 Gyr of thermal evolution. For our study we use cases 55 and 85 from Plesa et al. (2018)[77] and an additional case (Moho_2800) that has a crustal structure that agrees with the seismic observations of InSight[64]. The most important parameters of the geodynamical models are listed in

Supplementary Table **S4**. For a more detailed list of parameters, we refer to the corresponding publications indicated in the footnotes of

Supplementary Table **S4**. In the following, cases 55, 85, and Moho_2800 will be referred to as T_{cold}, T_{85}, and T_{hot}, respectively. The average present day temperature profiles for the 3 cases are shown in Supplementary Figure S4 together with the temperature range deduced from seismic and geodesy data[17]. T_{cold} and T_{hot} are situated close to the lower and upper limit of the seismically deduced temperature range but have a lithosphere thickness that is in the upper range of the latter.

Case	D_{mantle} [km]	η_{ref} [Pa s]	E [kJ/mol]	V [cm^3/mol]	D_{crust} [km]	ρ_{crust} [kg m^{-3}]	HPE_{crust} [%]
55[1] (T_{cold})	1700	1e20	300	6	87.1	3200	93.5
85[1] (T_{85})	1550	1e21	325	10	62	3100	67.8
Moho_2800[2] (T_{hot})	1550	1e21.5	300	6	62.2	2800	61.4

Supplementary Table S4: Parameters of the geodynamical thermal evolution models. The mantle thickness is given by D_{mantle}, the reference viscosity is indicated by η_{ref}, D_{crust} describes the average crustal thickness, while ρ_{crust} and HPE_{crust} indicate the crustal density and crustal amount of heat producing elements. 1: Plesa et al. (2018)[77]; 2: Knapmeyer-Endrun et al. (2021)[64].

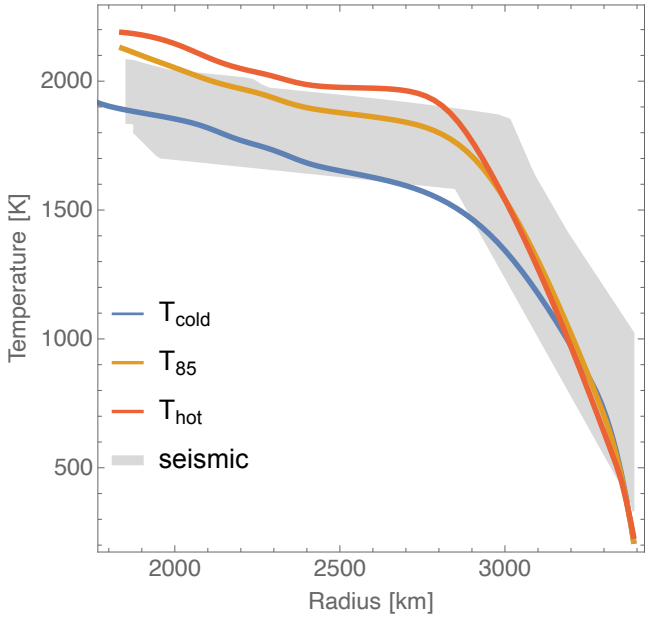

Supplementary Figure S4: Temperature profiles from this study (T_{cold}, T_{85}, and T_{hot})[64,77] and temperature range deduced from geodesy and seismic data[17].

The degree 2 present-day temperature anomalies associated with cases 55, 85, and Moho_2800 are shown in Supplementary Figure S5 (a,b,c). Horizontal temperature fluctuations lead to density anomalies that can affect the shape of the core (Supp: Core shape of non-hydrostatic planet), which directly affects the moments of inertia of the core. The induced degree-2 density anomalies have been calculated from a spherical harmonic expansion of the temperature fields obtained from the 3D thermal evolution calculation for the YMD composition (see Supplementary Figure S5 (d,e,f)) using the software package SHtools[79].

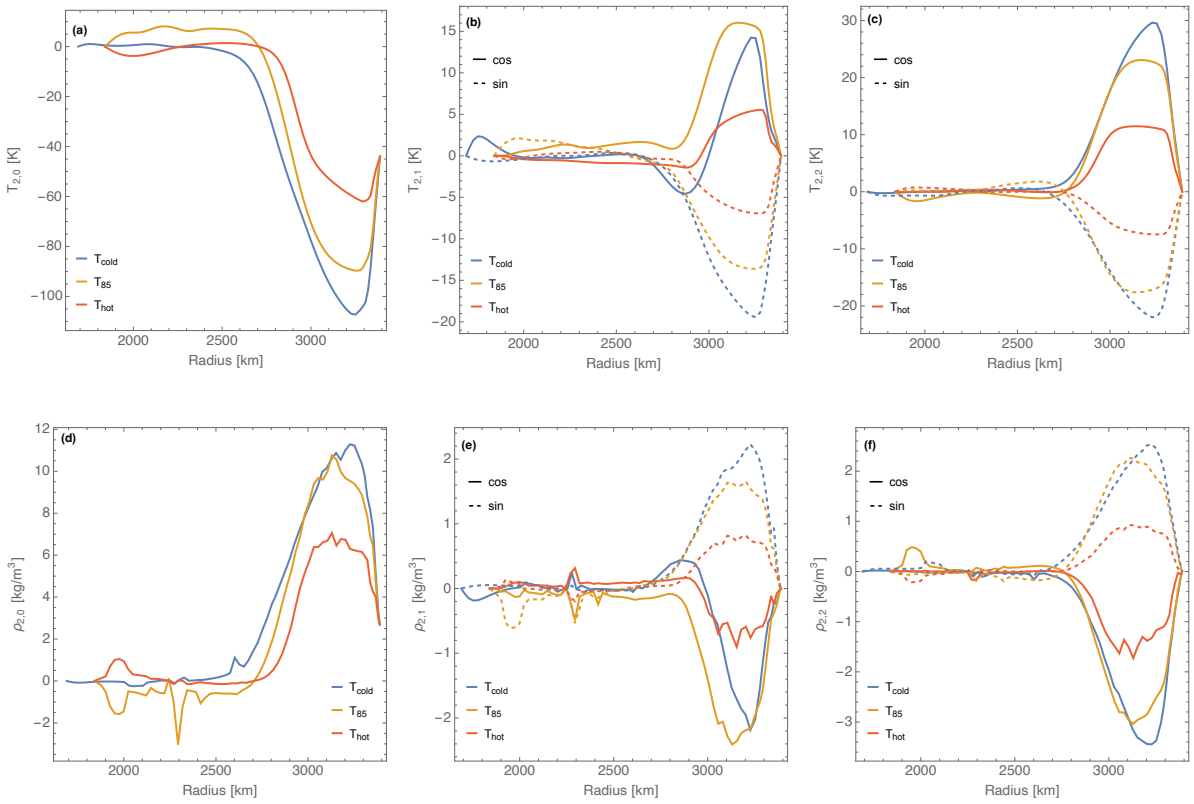

Supplementary Figure S5: Degree 2 and order (0,1,2) cos and sin horizontal temperature anomalies (a,b,c) and induced density anomalies (d,e,f) for the YMD mantle composition for the T_{cold}, T_{85}, and T_{hot} temperatures.

Section 8. Crustal structure

The crustal structure below the InSight lander inferred from seismic data can be used to constrain the thickness and density of the global crust when combined with gravity and topography data[64]. The deduced average crustal density and thickness are correlated and dependent on the density of the uppermost mantle[20,64].

The correlation between crustal thickness and density for the YMD and EH45 models have been calculated using the *ctplanet* software[63] and the results are shown in Supplementary Figure S6(a,b) and Supplementary Figure S7(a,b) for the 2- and 3- layer crust models compatible with seismic observations. The calculation of the average crustal thickness requires the knowledge of the thickness of the crust below the Insight lander. For both considered cases we use the seismically estimated thickness[64]; 20 ± 5 km for the 2-layer crust and 39 ± 8 km for 3-layer crust.

Only a subset of the interior structure models are found to agree with the moment of inertia of this study (Supplementary Figure S6(c,d) and Supplementary Figure S7(c,d)). Concerning the 2-layer InSight seismic model, only models based on the YMD composition with the hot mantle temperature agree with the moment of inertia. Nevertheless, since those models have a Love number k_2 that does not agree with observations[10], we do not consider them further in this study. Furthermore, we note that recent PP receiver function analyses strongly favor the 3-layer crustal model over the 2-layer model[80].

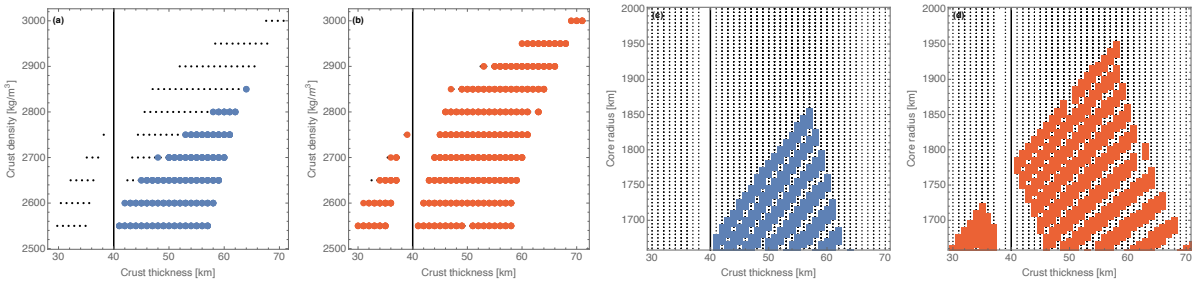

Supplementary Figure S6: Crust thickness-density correlation for T_{cold} (a) and T_{hot} (b) mantle temperatures and relation between crust thickness and core radius for mantle temperature T_{cold} (c) and T_{hot} (d) for the mantle composition YMD. The black vertical line delineates the 2 layered (thickness <40km) from the 3 layered (thickness >40km) crust models. Dots correspond to all crustal thickness models that are compatible with the InSight seismic thickness of the crust, whereas colored symbols correspond to the subset of models that are consistent with the moment of inertia.

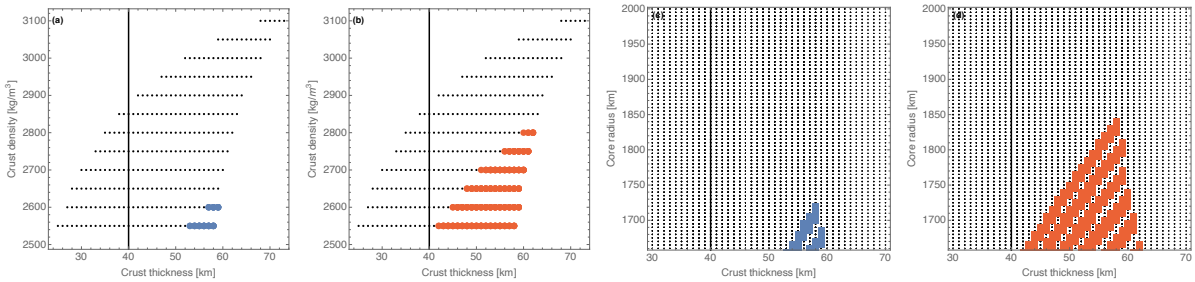

Supplementary Figure S7: Crust thickness-density correlation for T_{cold} (a) and T_{hot} (b) mantle temperatures and relation between crust thickness and core radius for mantle temperature T_{cold} (c) and T_{hot} (d) for the mantle composition EH45. The black vertical line delineates the 2 layered (thickness <40km) from the 3 layered (thickness >40km) crust models. Dots correspond to all crustal thickness models that are compatible with the InSight seismic thickness of the crust, whereas colored symbols correspond to the subset of models that are consistent with the moment of inertia.

Section 9. Anelasticity, triaxiality, CMB coupling, and Chandler wobble

The compliances β and γ required to compute the core amplification factor F and FCN period (Eq.3 of the main paper) are computed following Dehant and Mathews (2015)[3]. They are complex valued because the mantle of Mars behaves as an anelastic body at quasi-diurnal periods (nutation periods in the rotating frame). We use a frequency-dependent but depth-independent model of shear dissipation[e.g.59]. The parameters of the complex shear modulus are chosen such that the semi-diurnal tidal Love number k_2, the period of the Chandler Wobble, and the secular acceleration of Phobos agree with observations (Tab. S6 of Konopliv et al. (2020)[10]). The real parts of $\beta = (0.35 \pm 0.07)\ 10^{-3}$ and $\gamma = (1.46 \pm 0.15)10^{-3}$, as shown in Supplementary Figure S8. Mantle anelasticity reduces the FCN

period by about 2%, which is about 2 times larger than the uncertainty, and can be neglected for F, as its effect of less than 1% is small compared to the uncertainty.
The anelastic mantle also leads to a complex valued transfer function (Eq.2 of main paper), which results in the damping of the FCN resonance and to nutations that are out-of-phase with respect to the gravitational forcing. The (-3 degrees) out-of-phase contributions are smaller than 0.02 mas, which is two orders of magnitude smaller than what can be measured by RISE and are therefore neglected in this study.
Besides the anelastic mantle, the viscous coupling of the fluid core to the mantle and the irregular shape of the CMB can affect the period of the FCN of Mars (see Sec. 7.3.3 of Dehant and Mathews (2015)[3]). The effect of the former, which has been shown to affect the FCN frequency of the Earth by less than 0.1%[81,82], is neglected in our study. Topographic coupling is proportional to the square of the small topography at the core-mantle boundary[83], it is thus very small and neglected too.

The triaxiality of Mars affects its rotation. Including the effect increases the period of the Chandler Wobble (CW) by about 0.5 days[10] and it has a comparable effect on the FCN period, which decreases by less than 0.5 days (based on Eq.38 of Chen and Shen et al. (2007)[84]). The effect on the FCN is significantly smaller than biaxial non-hydrostatic contributions (>~7days) and can thus be neglected given the 2.7 days uncertainty on the FCN period. The precise effect of triaxiality on the core amplification factor F is currently unknown due to lacking theoretical developments. But it can be roughly estimated by calculating the effect of using the equatorial moments of inertia A or B instead of the average equatorial moment of inertia on F. We find, that F changes by about 2%, which is 5 times smaller than its 1σ uncertainty and is therefore neglected in our study.

Additional to the FCN, the CW rotational normal mode can affect nutation amplitudes (see Dehant and Mathews (2015)[3] Eq.7.140 for the full expression of the transfer function). Its period in the inertial frame is about -1.03 days[10], significantly smaller than any of the periods of the main rigid nutations[11] and as such is not expected to affect our results in a meaningful way. Using Eq.7.140 for the transfer function instead of Eq.3, shows that the amplitude of the -1/3 annual nutation is reduced by less than 0.5%, an effect that can be neglected given the 10% uncertainty on F.

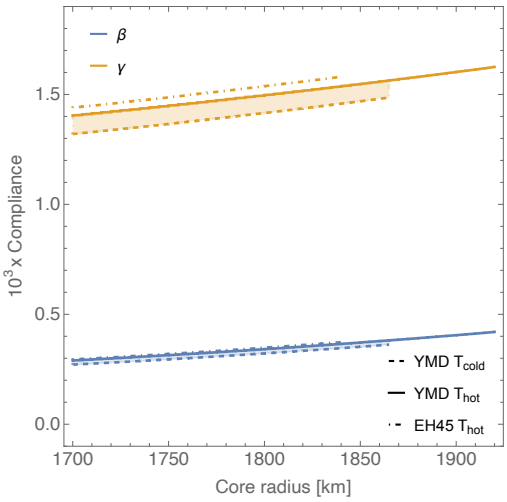

Supplementary Figure S8: Real part of compliance β and γ for the YMD mantle compositions and the cold (dashed lines) and hot (solid lines) mantle temperature and EH45 for the hot mantle temperature (dot-dashed lines)

Section 10. Core shape of non-hydrostatic planet

Nutation amplitudes depend on the shape of the planet and core mainly through the linear dependence of the FCN frequency on the dynamical flattening of the core (Eqs 2 and 3 of main text). The determination of the core shape of a non-hydrostatic planet requires assumptions about the rheology and about the internal processes generating non-hydrostatic deviations. In a purely static model, the external gravity field and shape of Mars can be explained by assuming that on a long time-scale Mars behaves like a fluid overlain by a solid shell (mechanical lithosphere) with embedded mass anomalies[20,85]. Compared to the fluid case, the FCN period of a non-hydrostatic planet with a 150 km thick shell is about 4% (10 days) shorter[20], which does not agree with RISE observations. Besides static

mass anomalies in the solid shell, the shape of the core can also be affected by dynamic processes in the fluid mantle resulting from mantle convection[22].
In the static model[20,85], the external shape and gravity field result from the rotational flattening, from the surface topography, and from mass sheet anomalies embedded in the mantle. The first static model is defined by one internal mass sheet located at the crust-mantle interface (Moho). The second static model is defined by one internal mass sheet located just above the bottom of the solid shell. In these two models, the FCN period will agree with the observations if the shell thickness is within a specific range. The third static model is defined by two internal mass sheets located at the Moho and just above the CMB in such a way that the deformation of the core is identical to the one of the hydrostatic model and as such in agreement with the FCN period measured by RISE.
We follow the approach of Zharkov et al. (2009)[85] to compute the deformation of the CMB due to loads. The procedure consists of four steps. In the first step, solving Clairaut's equation for a given interior model yields the reference hydrostatic shape and gravitational field[86]. Subtracting these from the surface data, we obtain the non-hydrostatic shape and the non-hydrostatic gravitational perturbation at the surface. In the second step, deformations at all depths and gravitational perturbations due to unit-value loads are computed with the well-known load Love number formalism[e.g.87]. We will first suppose that there are two static loads (surface topography and one internal load either at the Moho or at the bottom of the solid shell), and consider afterwards the case with three static loads. In the third step, the values of the two perturbing loads are determined so that the non-hydrostatic components of the shape and gravity field at harmonic degree 2 agree with data. In the fourth step, the moments of inertia of the core are computed by adding the hydrostatic and non-hydrostatic contributions. The diagonalization of the total inertia tensor yields the principal moments of inertia of the core.
If there are three static loads, the third load (located at the bottom of the mantle) is chosen so that the combined deformation of the three static loads on the core is consistent with the non-hydrostatic components of the core shape deduced from the RISE data. Since the non-hydrostatic components are close to zero (see Supp: Shape and moment of inertia of the core and Supplementary Figure S16), we choose the third load so that the effect of the two other loads is completely compensated.

In the dynamic model, the external shape and gravity field result from the perturbations of the static model with two loads, plus a third perturbation due to mantle convection. Mantle convection affects the core shape: its radial deformation is proportional to the discontinuity of the radial stress at the CMB[88]. In practice, viscous flow equations[89,90] are solved for density perturbations given by a 3D convection model (Supp: Thermal state of the mantle). The surface perturbations (radial and gravitational) due to convection are subtracted from both the observed gravity field and shape of the planet, along with the rotational perturbations in step 1 above. The procedure for calculating the core shape then follows the same course as for the static model. Finally, the deformation of the core-mantle boundary due to convection is added to the deformation due to the static loads before computing the moment of inertia of the core.

We illustrate the effect of the solid shell thickness on the shape of the core for the above loading schemes using an interior model based on the YMD composition and T_{hot} mantle temperature (Supp: Thermal state of the mantle). In this model, the core has a radius of 1815 km and the bottom of the thermal lithosphere is at a depth of 600 km, which corresponds to the largest shell thickness considered in this study. The results show that the thickness of the solid shell has only a small effect on the computed core shape if the load is placed at the depth of the Moho, while the deformation of the core decreases with increasing shell thickness when the load is placed at the bottom of the shell. The viscous flow in the convective mantle reduces the deformation of the core by about 50 m and this effect is only weakly dependent on the shell thickness. When loads are placed at the surface and Moho, the FCN period is predicted to be more than 10 days smaller than the RISE observation irrespective of the shell thickness (Supplementary Figure S9). When the second load is placed at the bottom of the solid shell, the FCN period matches the RISE observation only if it is thicker than about 512 km in the static setting, and about 426 km when dynamic convective effects are considered (viscous flow setting). The thinnest of these two values is comparable to the present-day elastic thickness beneath the north polar cap, which is predicted to lie between 330 and 450 km[91].

A comparison between the static and viscous flow setting for the interior structure models used in this study is shown in Supplementary Figure S10. Including the effect of viscous flow decreases the FCN period by about 5 days, which is comparable to the effect of changing the crust density from its highest to its lowest allowed value.

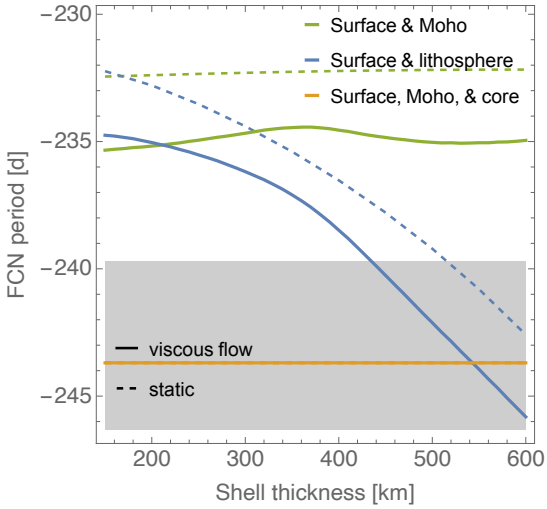

Supplementary Figure S9: FCN period as a function of shell thickness for loads placed at the surface and Moho, surface and bottom of the shell, and surface, Moho, and core for static (dashed curve) and viscous flow (solid curve) deformation. The gray shaded region represents the 1σ limits of the FCN period observed by RISE.

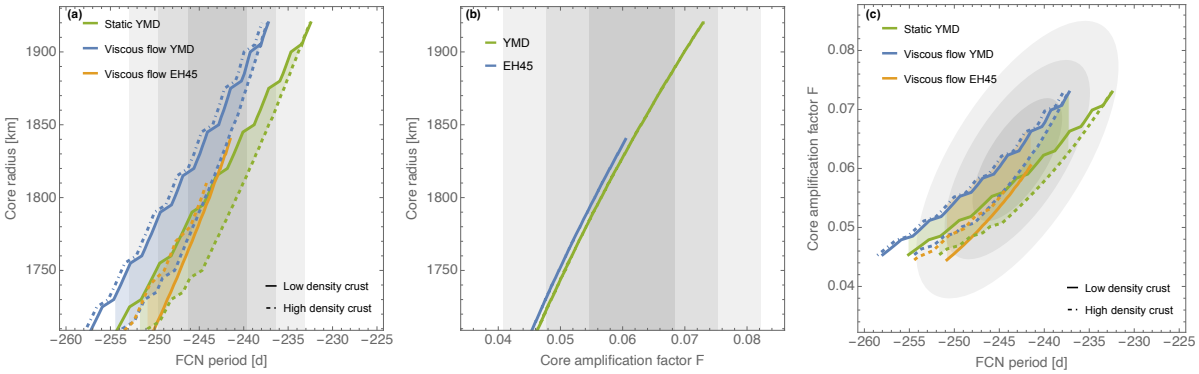

Supplementary Figure S10: (a) Core radius as a function of FCN period, (b) core radius as a function of core amplification factor, and (c) FCN period-core amplification correlation for the YMD and EH45 (only viscous flow) mantle composition and T_{hot} mantle temperature for loads placed at the surface and bottom of the lithosphere for the static and viscous flow setting. Solid and dashed curves represent models with an adiabatic core temperature and the dot-dashed curves assume an isothermal core temperature (thick crust+viscous flow). The gray shaded areas represent 1σ, 2σ, and 3σ uncertainties.

Section 11. Enriched basal silicate layer (BSL)

Like many terrestrial planets that differentiated into a metallic core and a silicate mantle, Mars probably experienced an early global magma ocean stage. The crystallization and the differentiation of a magma ocean can lead to the formation of a compositionally distinct layer at the bottom of the mantle[92], strongly enriched in heat-producing elements (HPE) and iron, leading to its long-term stability with little mixing between the layer and the overlying mantle[93,94,95]. The presence of an enriched basal silicate layer (BSL) can strongly affect the evolution of the planet and its current state. In particular, the basal layer can give rise to the presence of a molten silicate layer above the core that can act as a deep seismic reflector and be interpreted as an extension of the liquid core[23]. The relative rotation of this effective liquid core (metallic core + molten silicate layer) with respect to the mantle affects the nutation of Mars and as such is responsible for the signature of the core measured by RISE.

Following Samuel et al. (2019)[96] we compute the thermo-chemical evolution of a set of models that incorporate a BSL. The mantle is composed of a basal layer of thickness D_d enriched in iron and in heat producing elements that is overlain by a more depleted convecting mantle. The BSL is at least 10% denser than the overlying mantle and its density increases with depth, making it stable against convection. The insulating effect and the HPE enrichment of the BSL can lead to a partially or fully molten region in its lowermost part. If the melt fraction is above the critical value of 40%[101,102] the rheological behavior of that region is effectively that of a liquid, i.e. with a zero shear modulus. For smaller melt fractions, the partially molten region behaves as a soft, yet essentially solid (i.e., mushy) material of thickness D_{mush} with reduced but non-zero shear modulus. BSL models with a fully molten

lower part of thickness D_{liquid} have an apparent liquid core radius of $R_{liquid} = R_c + D_{liquid}$ that is compatible with the core radius range inferred from seismic data[17]. Following Drilleau et al. (2021)[103], we ascertained that our BSL models are also consistent with the differential arrival times (Supplementary Figure S11) of body waves (tS-tP, tPP-tP, tPPP-tP, tSSS-tS, tSS-tS, tScS-tS) observed by the seismometer on InSight[17,78] and their inferred locations[17] as well as the velocity structure in the 3 layered crust[64]. All models match the moment of inertia of Mars[10], have an average crustal thicknesses that is within the bounds inferred from receiver functions and gravity data[64], and are compatible with the recent volcanism observed for Mars[97,98].

BSL models require a liquid lower mantle layer to agree with the RISE observations. They have a thermal lithosphere between 260 km and about 315 km which are significantly thinner than those of the other models considered in this study. Therefore, the effect of a load placed at the bottom of the lithosphere on the FCN period is comparable to one placed at the Moho depth. Even with a load placed at a shallower depth, BSL models agree with the RISE data, mainly because the large core deformation induced by the Moho load (Supp: Core shape of non-hydrostatic planet) is strongly reduced by the compliance β (see Eq.3) because of the mushy lower mantle. Note that for all models considered, a lithosphere of the thickness of the thermal lithosphere has been assumed. The key governing parameters of our models are listed in Supplementary Table S5.
The apparent core radius of models with a fluid layer at the bottom of the mantle that are compatible with RISE agrees with the range deduced from models without a fluid basal layer from this study. RISE data cannot differentiate between models that have a thin or thick fluid basal layer.

Model	R_c [km]	D_d [km]	Tm_0 [K]	Tc_0 [K]	k_d [W/m/K]	V^* [cm^3/mol]	η_0 [Pa s]	D_{liquid} [km]	D_{mush} [km]	D_{solid} [km]
Rc1750_Dd100	1750	100	1800	2100	8	7	10^{21}	39	61	0
Rc1750_Dd100_kd6	1750	100	1700	2000	6	7	$3\ 10^{20}$	0	73	27
Rc1400_Dd200	1400	200	1800	2100	8	7	10^{21}	171	29	0
Rc1650_Dd200	1650	200	1800	2100	8	7	10^{21}	122	28	50
Rc1600_Dd300_kd4	1600	300	1800	2000	4	4	10^{21}	273	27	0
Rc1600_Dd300_kd16	1600	300	1800	2000	16	4	10^{21}	247	53	0
Rc1700_Dd300_kd4	1700	300	1800	2000	4	4	10^{21}	173	27	100

Supplementary Table S5: BSL models key parameters: Core radius (R_c), BSL thickness (D_d), initial uppermost mantle (Tm_0) and core temperatures (Tc_0), BSL thermal conductivity (k_d), effective activation volume (V^*) and reference viscosity (η_0) of the mantle, thicknesses of molten layer (D_{liquid}), mushy layer (D_{mush}), and solid layer (D_{solid}) within the BSL.

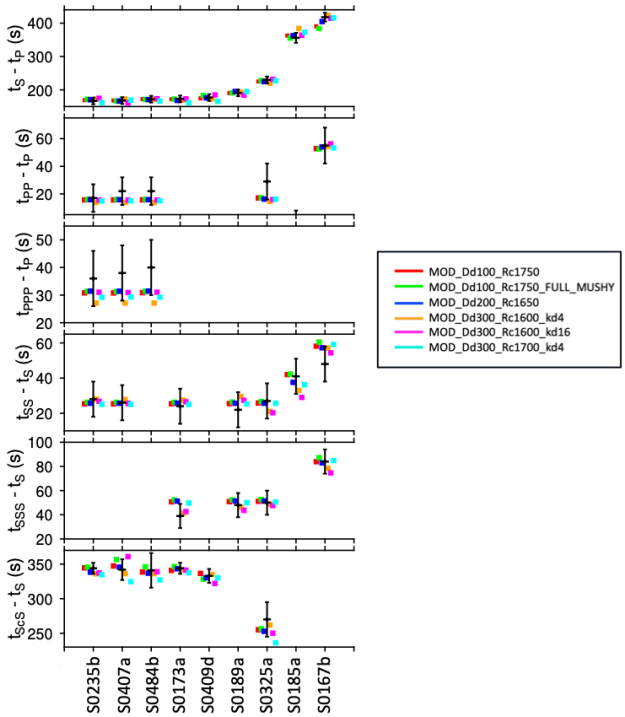

Supplementary Figure S11: Arrival times of the BSL models for the nine considered quakes (colored dots). The measured arrival times (black symbols) are shown with 1σ error-bars.

Section 12. Core structure and composition

The average density of the core of the models with the YMD or EH45 mantle compositions that agree with RISE are between about 5955-6290 kg/m^3 (Supplementary Figure S12a). This range is narrower than the 5700-6300 kg/m^3 range advocated by[17], and our lower bound is significantly higher. The main reason for this difference results from the uppermost mantle density that can be appreciably higher in models deduced from seismic data that are based on the so-called geophysical approach[17]. In this approach, a layer with constant density in the uppermost part of the mantle is modeled directly from the inferred seismic velocities[78] while density should vary with depth as the case if it were related to composition and temperature. Other less important factors that affect the density of the core result from the wider spread of mantle temperatures (Supp: Thermal state of the mantle) and the larger set of mantle compositions considered in Stähler et al. (2021)[17] (Lodders and Fegley (1997)[104], EH45[13], Taylor (2013)[105], YMD[14]). We don't use the models of Lodders and Fegley (1997)[104] and Taylor (2013)[105]since the latter does not agree with the crust structure and the moment of inertia of Mars and the former leads to results that are equivalent to those based on EH45[64]. Note that, given the mass conservation, the differences in mantle density directly reflect on the density jump at the core mantle boundary (Supplementary Figure S14). Models that agree with RISE data have a density jump of 1694-2108 kg/m^3. Because of the larger average core density found in this study, the required fraction of light elements in the core is appreciably lower than in Stähler et al. (2021) [17] (see their Fig. 2 and Fig. S11-1b) and in particular, up to 5 wt% O and 2 wt% H are not required if the amount of S is limited to the range deduced from cosmochemical considerations[25]. The fraction of O in the core increases with S, which increases with core radius (Supplementary Figure S13a), and is larger for EH45 models than YMD models since the former have a larger fraction of FeO in the mantle[26]. The amount of C that can dissolve in the core at core-mantle boundary conditions increases with decreasing amount of S (Supplementary Figure S13b) and is about two times larger if the core contains 1wt% of H. As a result of the required large fraction of S, the maximal amount of C that can dissolve in the core is below predictions based on an assumed bulk C content (e.g. 1-1.4wt%[25]) and its partitioning behavior between molten metal and silicate ($log\ (D_C{}^{met-sil})\sim 0.5-2.5$[57,106]) at core-mantle boundary conditions (Supplementary Figure S13b). The precise temperature profile in the core is not known and is likely between an isotherm and adiabat[e.g.52]. Using an isothermal temperature profile in the core increases the fraction of light elements by up to about 0.5 wt% if compared to a calculation with an adiabatic temperature profile. The effect of this difference in light elements decreases the density jump at the CMB by less than 3% and decreases the moment of inertia of the core by less than 0.2%. Those combined effects decrease the FCN period by up to 0.6 day (Supplementary Figure S10) and increase F by up to 0.3%. Since those effects are small compared to the uncertainties at 1σ, for convenience we assume an adiabatic temperature profile in the core for the calculation of the FCN period and F and for the discussion related to the composition of the core.

The large fraction of light elements in the core (Figure 4 of main paper, Supplementary Figure S13) makes the presence of an inner core highly unlikely. The melting temperature of Fe-O-S-C-H alloys at Mars core conditions is not well known, but an upper bound can be roughly estimated by cumulating the effect that each individual light element has on the melting temperature of Fe. As long as the composition of the alloy is on the iron-rich side of the eutectic, the addition of light elements to Fe results in a decrease of its melting temperature. If the core has a radius of 1835 km, as found in this study, about 2.5 wt%O, 15 wt%S, 1.5 wt%C, and 1 wt%H are required to match its density. At core center pressures (~40 GPa), adding 15 wt% of S decreases the melting temperature of Fe (2800 K[107]) by ~1000 K[108], whereas individually 2.5 wt%O, 1.5 wt%C, and 1 wt%H result in temperature reductions of ~250 K[67], ~255 K[109] and ~220 K[110], respectively. The cumulative effect of all those light elements results in a melting temperature at the center of the core that is significantly below the core temperature (1880 K - 2400 K).

The amount of light elements in the core can be lower if the mantle is less dense than assumed above, for example by having a lower FeO content or a higher temperature. Temperatures significantly above our hot end-member model are, however, unlikely (Supp: Thermal state of the mantle) and the effect of decreasing the weight fraction of FeO in the mantle has only a small effect of the order of 1 wt% on the amount of light elements (main text Fig. 4), as follows from a comparison of the EH45 and YMD models (17.7 wt% vs. 14.7 wt% FeO in the mantle). We nevertheless note that the effect of the lower amount of FeO in the mantle is reduced by the more massive crust of the YMD models compared with EH45 models (Supp: Crustal structure) and the tradeoff between mantle FeO and O-S content in the core[26].

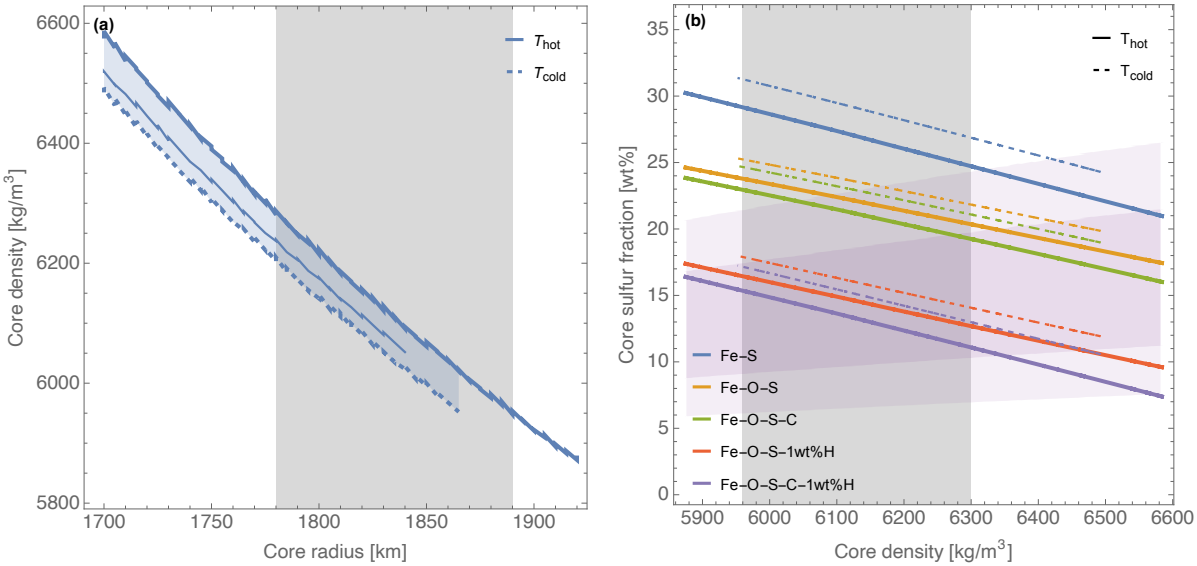

Supplementary Figure S12: (a) Average core density as a function of core radius for the YMD mantle composition with the T_{hot} and T_{cold} mantle temperatures (thick lines) and for the EH45 mantle composition with the T_{hot} temperature profile (thin line). The gray area represents the core radius of this study (1σ). (b) Relation between core density and core composition for the YMD mantle composition and the T_{hot} and T_{cold} temperature profiles. The gray array represents the core density range that agrees with the core radius of this study. The light purple area is the core S content following cosmochemical considerations[25] and the lighter purple area assumes that the S content of Mars is equivalent to chondrites (1.6-5.6 wt%)[32].

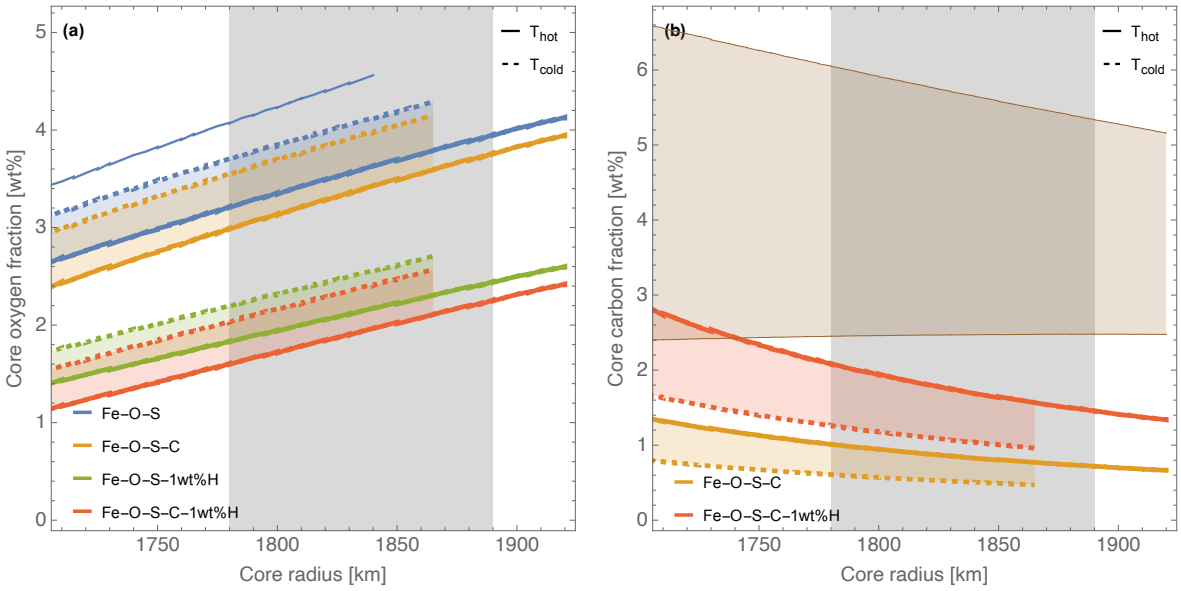

Supplementary Figure S13: Core oxygen (a) and carbon fraction at its solubility limit at core-mantle boundary conditions (b) for T_{hot} and T_{cold}. The gray area represents the core radius of this study (1σ). YMD models are represented by the thick curve and the thin curve represents the EH45 models with the T_{hot} profile. The brownish area in (b) represents the C content in the core assuming a bulk content range and the partition behavior of C between the liquid core and molten mantle at core-mantle boundary conditions (see text).

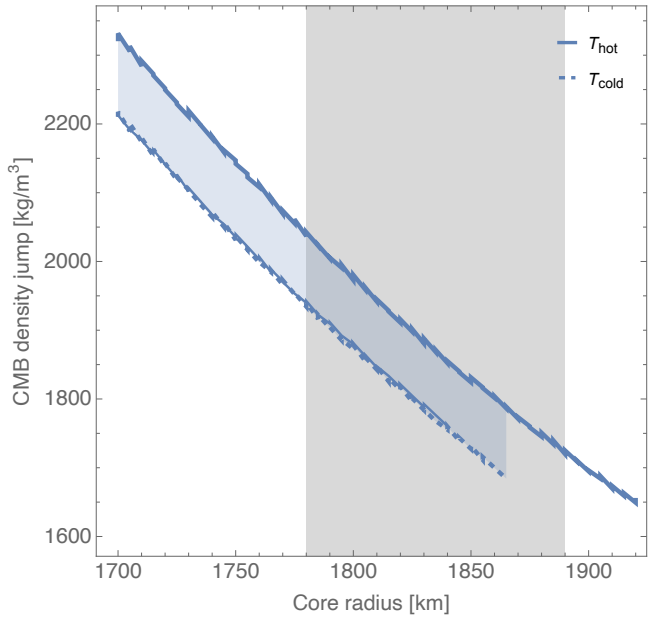

Supplementary Figure S14: Density jump at the CMB for the T_{hot} and T_{cold}. The gray area represents the core radius of this study (1σ). YMD models are represented by the thick curves and the thin curve represents the EH45 models with the T_{hot} profile.

Section 13. Shape and moment of inertia of the core

The moment of inertia of the core can be obtained from F (Eq.3 in the main paper) but it requires to know the compliance γ. Forward modeling shows that the models of this study and models with a dense fluid lower mantle layer (Supp: Core structure and composition) have a γ between $1.4 \cdot 10^{-3}$ and $1.62 \cdot 10^{-3}$ if they agree with the k_2 Love number at 1σ. We can take into account our lack of knowledge about γ if we assume that it is a random variate with an uniform distribution between $1.4 \cdot 10^{-3}$ and $1.62 \cdot 10^{-3}$. The moment of inertia of the core can then be estimated by Monte Carlo error propagation if we assume that F and the principal moments of inertia of Mars have a normal distribution around their mean value. We find that $A_f/m_a\, {r_a}^2 = 0.0286 \pm 0.0033$ (11%). The moment of inertia of the core of our interior models is shown in (Supplementary Figure S15).

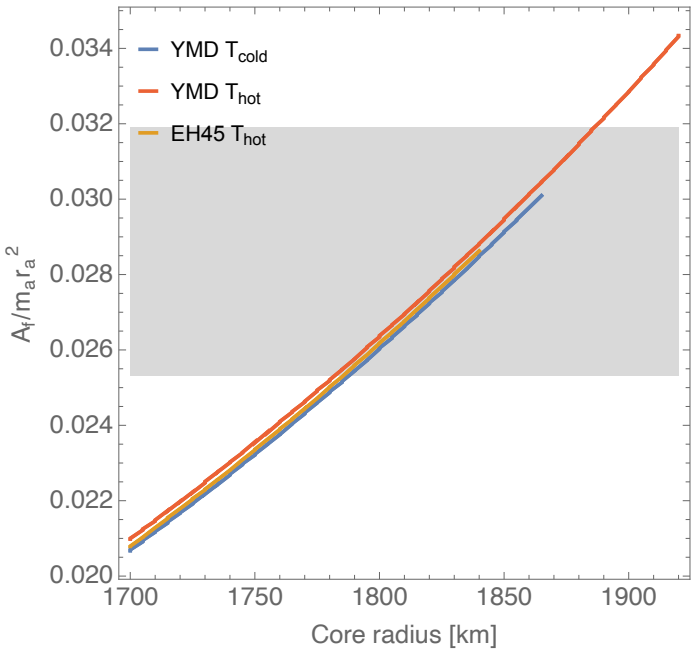

Supplementary Figure S15: Normalized core moment of inertia for the YMD composition with the hot and cold temperature and EH45 composition with the hot mantle temperature. The gray shaded area represents the value of A_f estimated from F (1σ).

The dynamical core flattening e_f of the Mars models used in this study can be estimated from the measured FCN period and compliance β using (Eq.3 of the main paper). Models that agree with the core flattening (Supp: Core shape of non-hydrostatic planet) require either a thick lithosphere with a mass anomaly placed at the bottom or at the Moho and bottom of the mantle (see Supplementary Figure S16) both together with the load induced by the crust at the surface. Note that for the latter case the load at the bottom of the mantle is set such that the combined deformation of the surface and Moho load on the core is cancelled, i.e. the core has the shape of a hydrostatic planet.

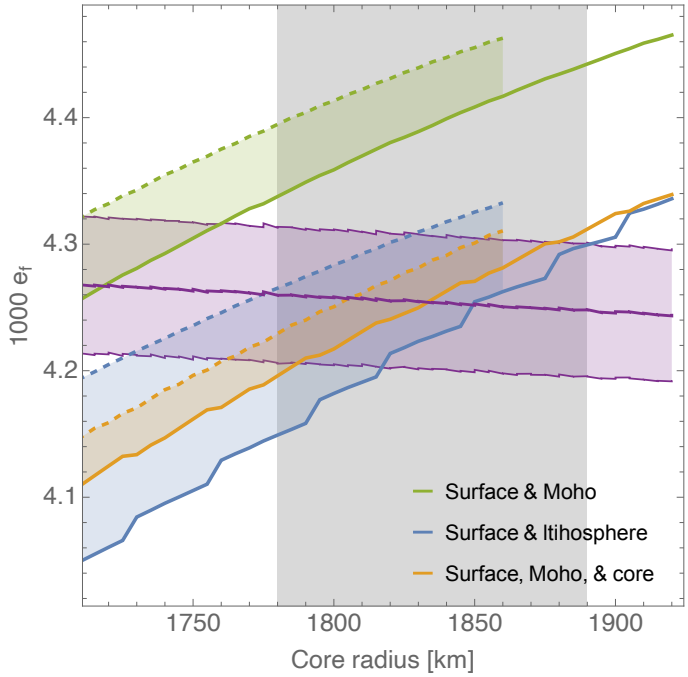

Supplementary Figure S16: Dynamic core flattening in agreement with RISE data as a function of core radius (purple area) compared to models with the YMD mantle composition that have loads at the surface & Moho, surface & lithosphere, and surface, Moho & core. Dashed curves represent models with the hot temperature profile and dashed curves are for cold temperature. The gray shaded area represents the core radius deduced from the core amplification factor F of this study (1σ). Models with loads placed at the surface, Moho & core have the core flattening of a hydrostatic planet.

Supplementary references

1. W. B. Banerdt, S. E. Smrekar, D. Banfield, D. Giardini, M. Golombek, C. L. Johnson, P. Lognonné, A. Spiga, T. Spohn, C. Perrin, S. C. Stähler, D. Antonangeli, S. Asmar, C. Beghein, N. Bowles, E. Bozdag, P. Chi, U. Christensen, J. Clinton, G. S. Collins, I. Daubar, V. Dehant, M. Drilleau, M. Fillingim, W. Folkner, R. F. Garcia, J. Garvin, J. Grant, M. Grott, J. Grygorczuk, T. Hudson, J. C. E. Irving, G. Kargl, T. Kawamura, S. Kedar, S. King, B. Knapmeyer-Endrun, M. Knapmeyer, M. Lemmon, R. Lorenz, J. N. Maki, L. Margerin, S. M. McLennan, C. Michaut, D. Mimoun, A. Mittelholz, A. Mocquet, P. Morgan, N. T. Mueller, N. Murdoch, S. Nagihara, C. Newman, F. Nimmo, M. Panning, W. T. Pike, A.-C. Plesa, S. Rodriguez, J. A. Rodriguez-Manfredi, C. T. Russell, N. Schmerr, M. Siegler, S. Stanley, E. Stutzmann, N. Teanby, J. Tromp, M. van Driel, N. Warner, R. Weber, M. Wieczorek, Initial results from the InSight mission on Mars. *Nat. Geosci.* **13**, 183–189 (2020).

2. W.M. Folkner, V. Dehant, S. Le Maistre, M. Yseboodt, A. Rivoldini, T. Van Hoolst, S.W. Asmar, M.P. Golombek, The rotation and interior structure experiment on the InSight mission to Mars. *Space Sci. Rev.* **214** (5), 100 (2018).

3. V. Dehant, V., P.M. Mathews, Ed., Precession, Nutation and Wobble of the Earth, *Cambridge University Press*, Cambridge (2015).

4. T. Sasao, S. Okubo, M. Saito, A simple theory on dynamical effects of stratified fluid core upon nutational motion of the Earth, *Proc. IAU Symposium* **78**, 165–183 (1980).

5. W.M. Folkner, C.F. Yoder, D.N. Yuan, E.M. Standish, R.A. Preston, Interior structure and seasonal mass redistribution of Mars from radio tracking of Mars pathfinder. *Science* **278** (5344), 1749–1752 (1997).

6. C.F. Yoder, E.M. Standish, Martian precession and rotation from Viking lander range data. *J. Geophys. Res.* **102**(E2), 4065–4080 (1997).

7. S. Evans, W. Taber, T. Drain, J. Smith, H.-C. Wu, M. Guevara, R. Sunseri, J. Evans, MONTE: The next generation of mission design and navigation software. *CEAS Space J.* **10**, 79–86 (2018).

8. J.C. Marty, S. Loyer, F. Perosanz, F. Mercier, G. Bracher, B. Legresy, L. Portier, H. Capdeville, F. Fund, J.M. Lemoine, GINS: The CNES/GRGS GNSS scientific software, *In 3rd Int. Coll. Sci. Fundam. Asp. Galileo Program. ESA proceedings WPP326* **31**, 8-10 (2011).

9. S. Le Maistre, P. Rosenblatt, A. Rivoldini, V. Dehant, J.-C. Marty, O. Karatekin, Lander radio science experiment with a direct link between Mars and the Earth. *Planet. Space Sci.* **68**, 105–122 (2012).

10. A. S. Konopliv, R. S. Park, A. Rivoldini, R.-M. Baland, S. Le Maistre, T. Van Hoolst, M. Yseboodt, V. Dehant, Detection of the Chandler Wobble of Mars From Orbiting Spacecraft. *Geophys. Res. Lett.* **47**, e2020GL090568 (2020).

11. R.-M. Baland, M. Yseboodt, S. Le Maistre, A. Rivoldini, T. Van Hoolst, V. Dehant, The precession and nutations of a rigid Mars. *Celest Mech Dyn Astr* **132**, 47 (2020).

12. D. Banfield, J.A. Rodriguez-Manfredi, C.T. Russell, K.M. Rowe, D. Leneman, H.R. Lai, P.R. Cruce, J.D. Means, C.L. Johnson, S.P. Joy, P.J. Chi, I.G. Mikellides, S. Carpenter, S. Navarro, E. Sebastian, J. Gomez-Elvira, J. Torres, L. Mora, V. Peinado, A. Lepinette, K. Hurst, P. Lognonné, S.E. Smrekar, W.B. Banerdt, InSight Auxiliary Payload Sensor Suite (APSS). *Space Sci. Rev.* **215**(1), 1-33 (2019).

13. C. Sanloup, F.Guyot, P. Gillet, G. Fiquet, M. Mezouar, I. Martinez, Density measurements of liquid Fe-S alloys at high pressure. *Geophys. Res. Lett.* **27**, 811 (1999).

14. T. Yoshizaki, W. F. McDonough, The composition of Mars, *Geochim. Cosmochim. Acta* **273**, 137–162 (2020).

15. S.E. Smrekar, P. Lognonné, T. Spohn, W.B. Banerdt, D. Breuer, U. Christensen, V. Dehant, M. Drilleau, W. Folkner, N. Fuji, R.F. Garcia, D. Giardini, M. Golombek, M. Grott, T. Gudkova, C. Johnson, A. Khan, B. Langlais, A. Mittelholz, A. Mocquet, R. Myhill, M. Panning, C. Perrin, W.T. Pike, A.C. Plesa, A. Rivoldini, H. Samuel, S. Staehler, T. Van Hoolst, M. van Driel, O. Verhoeven, R. Weber, M. Wieczorek, Pre-mission InSights on the Interior of Mars. *Space Sci Rev.* **215**, 3 (2019).

16. C. F. Yoder, A. S. Konopliv, D. N. Yuan, E. M. Standish, W. M. Folkner, Fluid core size of Mars from detection of the solar tide. *Science* **300,** 299–303 (2003).

17. S. C. Stähler, A. Khan, W. B. Banerdt, P. Lognonné, D. Giardini, S. Ceylan, M. Drilleau, A. C. Duran, R. F. Garcia, Q. Huang, D. Kim, V. Lekic, H. Samuel, M. Schimmel, N. Schmerr, D. Sollberger, É. Stutzmann, Z. Xu, D. Antonangeli, C. Charalambous, P. Davis, J. C. E. Irving, T. Kawamura, M. Knapmeyer, R. Maguire, A. G. Marusiak, M. P. Panning, C. Perrin, A.-C. Plesa, A. Rivoldini, C. Schmelzbach, G. Zenhäusern, É. Beucler, J. Clinton, N. Dahmen, M. van Driel, T. Gudkova, A. Horleston, W. T. Pike, M. Plasman, S. E. Smrekar, Seismic detection of the martian core. *Science* **373**, 443–448 (2021).

18. A. Rivoldini, T. Van Hoolst, O. Verhoeven, A. Mocquet, V. Dehant, Geodesy constraints on the interior structure and composition of Mars. *Icarus* **213**, 451–472 (2011).

19. A. Khan, C. Liebske, A. Rozel, A. Rivoldini, F. Nimmo, J. A. D. Connolly, A.-C. Plesa, D. Giardini, A geophysical perspective on the bulk composition of Mars. *J. Geophys. Res.* **123**, 575–611 (2018).

20. M. A. Wieczorek, M. Beuthe, A. Rivoldini, T. Van Hoolst, Hydrostatic interfaces in bodies with nonhydrostatic lithospheres. *J. Geophys. Res. Planets* **124**, 1410–1432 (2019).

21. W.S. Kiefer, B.G. Bills, R.S. Nerem, An inversion of gravity and topography for mantle and crustal structure on Mars. *J. Geophys. Res. Planets* ***101***, 9239 (1996).

22. P. Defraigne, V. Dehant, T. Van Hoolst, Steady-state convection in Mars' mantle. *Planet. Space Sci.*, **49**, 501–509 (2001).

23. H. Samuel, M. D. Ballmer, S. Padovan, N. Tosi, A. Rivoldini, A.-C. Plesa, The Thermo-Chemical Evolution of Mars With a Strongly Stratified Mantle. *J. Geophys. Res. Planets* **126**, e2020JE006613 (2021).

24. A. K. McNamara, A review of large low shear velocity provinces and ultra low velocity zones. *Tectonophysics* **760**, 199–220 (2019).

25. E. S. Steenstra, W. van Westrenen, A synthesis of geochemical constraints on the inventory of light elements in the core of Mars. *Icarus* **315**, 69–78 (2018).

26. H. Gendre, J. Badro, N. Wehr, S. Borensztajn, Martian core composition from experimental high-pressure metal-silicate phase equilibria. *Geochemical Perspectives Letters*, *21*, 42-46 (2022).

27. Y. Shibazaki, E. Ohtani, H. Terasaki, A. Suzuki, K. Funakoshi, Hydrogen partitioning between iron and ringwoodite: Implications for water transport into the Martian core. *Earth Planet. Sci. Lett.* **287**, 463–470 (2009).

28. V.N. Zharkov, The Internal Structure of Mars: A Key to Understanding the Origin of Terrestrial Planets, *Sol. Syst. Res.* **30**, 456-46 (1996).

29. K. Tsuno, D.J Frost, D.C. Rubie, The effects of nickel and sulphur on the core-mantle partitioning of oxygen in Earth and Mars. *Phys. Earth Planet. Inter.* **185**, 1–12 (2011).

30. P. Defraigne, A. Rivoldini, T. Van Hoolst, V. Dehant, Mars nutation resonance due to free inner core nutation. *J. Geophys. Res., Planets* **108**(E12), 5128 (2003).

31. A. Mittelholz, C. L. Johnson, J. M. Feinberg, B. Langlais, R. J. Phillips, Timing of the martian dynamo: New constraints for a core field 4.5 and 3.7 Ga ago. *Sci. Adv.* **6**, 18 (2020).

32. K. Lodders, Relative atomic solar system abundances, mass fractions, and atomic masses of the elements and their isotopes, composition of the solar photosphere, and compositions of the major chondritic meteorite groups. *Space Sci Rev*, **217**(3), 44 (2021).

33. J.A. Estefan and O.J. Sovers, JPL Publication **94-24** (1994)

34. S. Le Maistre, Martian Lander Radio Science Data Calibration for Mars Troposphere. *Radio Science*, **55**(12), 1–16 (2020).

35. D. Buccino, J.S. Border, W.M. Folkner, D. Kahan, S. Le Maistre, Low-SNR Doppler Data Processing for the InSight Radio Science Experiment. *Remote Sensing*. **14**(8), 1924 (2022).

36. S. Le Maistre, P. Rosenblatt, V. Dehant, J.-C. Marty, M. Yseboodt, Mars rotation determination from a moving rover using Doppler tracking data: What could be done? *Planet. Space Sci.* **159**, 17-27 (2018).

37. W. M. Folkner, J. G. Williams, D. H. Boggs, R. S. Park, P. Kuchynka, The planetary and lunar ephemerides DE430 and DE431, *Interplanetary Network Progress Rep.* **42,** 196 (2014).

38. R. A. Jacobson, V. Lainey, Martian satellite orbits and ephemerides. *Planetary and Space Science*. **102**, 35-44 (2014).

39. V. Dehant, P. Defraigne, and T. Van Hoolst, Computation of Mars' transfer functions for nutations, tides and surface loading. *Physics of the Earth and Planetary Interiors*, **117,** 385–395, January 2000.

40. T. Van Hoolst, V. Dehant, F. Roosbeek, and P. Lognonné, Tidally induced surface displacements, external potential variations, and gravity variations on Mars. *Icarus*, **161**, 281–296, 2 2003.

41. B. A. Archinal, C. H. Acton, M. F. A'Hearn, A. Conrad, G. J. Consolmagno, T. Duxbury, D. Hestroffer, J. L. Hilton, R. L. Kirk, S. A. Klioner, D. McCarthy, K. Meech, J. Oberst, J. Ping, P. K. Seidelmann, D. J. Tholen, P. C. Thomas, I. P. Williams, Report of the IAU Working Group on Cartographic Coordinates and Rotational Elements: 2015. *Celestial Mech. Dyn. Astron.* **130**, 22 (2018).

42. A.S. Konopliv, C.F. Yoder, E.M. Standish, D.-N. Yuan, W.L. Sjogren, A global solution for the Mars static and seasonal gravity, Mars orientation, Phobos and Deimos masses, and Mars ephemeris. *Icarus* **182**(1), 23–50 (2006).

43. V. Dehant, S. Le Maistre, R.-M. Baland, Ö. Karatekin, M.-J. Péters, A. Rivoldini, T. van Hoolst, M. Yseboodt, M. Mitrovic, the LaRa team, The radioscience LaRa instrument onboard ExoMars 2020 to investigate the rotation and interior of Mars. *Planetary and Space Science*, **180**, 104776 (2020).

44. D. Kahan, W. M. Folkner, D. R. Buccino, V. Dehant, S. Le Maistre, A. Rivoldini, T. Van Hoolst, M. Yseboodt, J. C. Marty, Mars precession rate determined from radiometric tracking of the InSight lander. *Planet. Space Sci.* **199**, 105208 (2021).

45. R.-M. Baland, A. Hees, M. Yseboodt, A. Bourgoin, S. Le Maistre, Relativistic contributions to the rotation of Mars. *Astronomy and Astrophysics*, **670**, A29 (2023).

46. L. Lange, F. Forget, D. Banfield, M. Wolff, A. Spiga, E. Millour, D. Viúdez-Moreiras, A. Bierjon, S. Piqueux, C. Newman, J. Pla-García, W.B. Banerdt, Insight pressure data recalibration, and its application to the study of long-term pressure changes on mars. *J. Geophys. Res., Planets* **127** (2022).

47. J.M. de la Torre, S. Piqueux, D.M. Kass, C. Newman, S.D. Guzewich, Pressure Deficit in Gale Crater and a Larger Northern Polar Cap after the Mars Year 34 Global Dust Storm. In *AGU Fall Meeting Abstracts*, **2019**, P51C-02 (2019).

48. P. Kuchynka, W.M. Folkner, A.S. Konopliv, R.S. Park, S. Le Maistre, V. Dehant, New constraints on Mars rotation determined from radiometric tracking of the opportunity Mars exploration rover. *Icarus* **229**, 340–347 (2014).

49. M. P. Panning, P. Lognonné, W. Bruce Banerdt, R. Garcia, M. Golombek, S. Kedar, B. Knapmeyer-Endrun, A. Mocquet, N. A. Teanby, J. Tromp, R. Weber, E. Beucler, J.-F. Blanchette-Guertin, E. Bozdağ, M. Drilleau, T. Gudkova, S. Hempel, A. Khan, V. Lekić, N. Murdoch, A.-C. Plesa, A. Rivoldini, N. Schmerr, Y. Ruan, O. Verhoeven, C. Gao, U. Christensen, J. Clinton, V. Dehant, D. Giardini, D. Mimoun, W. Thomas Pike, S. Smrekar, M. Wieczorek, M. Knapmeyer, J. Wookey, Planned products of the Mars structure service for the InSight mission to Mars. *Space Sci. Rev.* **211**, 611–650 (2016).

50. J. A. D.Connolly, Computation of phase equilibria by linear programming: a tool for geodynamic modeling and its application to subduction zone decarbonation. *Earth Planet. Sci. Lett.* **236**, 524–541 (2005).

51. L. Stixrude, C. Lithgow-Bertelloni, Thermodynamics of mantle minerals. Part 1: Physical properties. *Geophys. J. Int.* **162**, 610–632 (2005).

52. S. Greenwood, C.J. Davies, A. Pommier, Influence of Thermal Stratification on the Structure and Evolution of the Martian Core. *Geophysical Research Letters*, **48**(22), e2021GL095198 (2021).

53. H. Terasaki, A. Rivoldini, Y. Shimoyama, K. Nishida, S. Urakawa, M. Maki, F. Kurokawa, Y. Takubo, Y. Shibazaki, T. Sakamaki, A. Machida, Y. Higo, K. Uesugi, A. Takeuchi, T. Watanuki, T. Kondo, Pressure and Composition Effects on Sound Velocity and Density of Core-Forming Liquids: Implication to Core Compositions of Terrestrial Planets. *J. Geophys. Res. Planets* **124**, 2272–2293 (2019).

54. K. Tsuno, D. S. Grewal, R. Dasgupta, Core-mantle fractionation of carbon in Earth and Mars: The effects of sulfur. *Geochim. Cosmochim. Acta* **238**, 477–495 (2018).

55. T. Okuchi, Hydrogen partitioning into molten iron at high pressure: implications for Earth's core. *Science* **278**, 1781–1784 (1997).

56. V. Clesi, M. A. Bouhifd, N. Bolfan-Casanova, G. Manthilake, F. Schiavi, C. Raepsaet, H. Bureau, H. Khodja, D. Andrault, Low hydrogen contents in the cores of terrestrial planets. *Sci. Adv.* **4**, e1701876 (2018).

57. V. Malavergne, H. Bureau, C. Raepsaet, F. Gaillard, M. Poncet, S. Surblé, D. Sifré, S. Shcheka, C. Fourdrin, D. Deldicque, H. Khodja, Experimental constraints on the fate of H and C during planetary core-mantle differentiation. Implications for the Earth. *Icarus* **321**, 473-485 (2019).

58. L. Yuan, G. Steinle-Neumann, Strong sequestration of hydrogen into the Earth's core during planetary differentiation. *Geophys. Res. Lett.* **47**, e2020GL088303 (2020).

59. D.L. Anderson, J.B. Minster, The frequency dependence of Q in the Earth and implications for mantle rheology and Chandler wobble. *Geophys. J. R. Astron. Soc.* **58**, 431–440 (1979).

60. M. Yseboodt, V. Dehant, M.J. Péters, Signatures of the Martian rotation parameters in the Doppler and range observables. *Planet. Space Sci*. **144**, 74–88 (2017).

61. M. Yseboodt, R.M. Baland, S. Le Maistre, Mars orientation and rotation angles, *Celest Mech Dyn Astr.* submitted (2023).

62. A. S. Konopliv, R. S. Park, W. M. Folkner. An improved JPL Mars gravity field and orientation from Mars orbiter and lander tracking data. *Icarus* **274**, 253–260 (2016).

63. M. Wieczorek, Create crustal thickness maps of planets from gravity and topography (ctplanet). doi:10.5281/zenodo.4439426 (2021).

64. B. Knapmeyer-Endrun, M. P. Panning, F. Bissig, R. Joshi, A. Khan, D. Kim, V. Lekić, B. Tauzin, S. Tharimena, M. Plasman, N. Compaire, R. F. Garcia, L. Margerin, M. Schimmel, E. Stutzmann, N. Schmerr, E. Bozdağ, A.-C. Plesa, M. A. Wieczorek, A. Broquet, D. Antonangeli, S. M. McLennan, H. Samuel, C. Michaut, L. Pan, S. E. Smrekar, C. L. Johnson, N. Brinkman, A. Mittelholz, A. Rivoldini, P. M. Davis, P. Lognonné, B. Pinot, J. Scholz, S. Stähler, M. Knapmeyer, M. van Driel, D. Giardini, W. B. Banerdt, Thickness and structure of the martian crust from InSight seismic data. *Science* **373**, 438–443 (2021).

65. E. C. Thompson, A. H. Davis, W. Bi, J. Zhao, E. E. Alp, D. Zhang, E. Greenberg, V. B. Prakapenka, A. J. Campbell, High-Pressure Geophysical Properties of fcc Phase FeH_x. *Geochem. Geophys. Geosys.* **19**, 305–314 (2018).

66. P.I. Dorogokupets, A.M. Dymshits, K.D. Litasov, T.S. Sokolova, Thermodynamics and Equations of State of Iron to 350 GPa and 6000 K. *Sci. Rep.* **7**, 41863 (2017).

67. T. Komabayashi, Thermodynamics of melting relations in the system Fe-FeO at high pressure: Implications for oxygen in the Earth's core. *J. Geophys. Res.* **119**, 4164–4177 (2014).

68. F. Xu, G. Morard, N. Guignot, A. Rivoldini, G. Manthilake, J. Chantel, L. Xie, A. Yoneda, A. King, E. Boulard, S. Pandolfi, F.J. Ryerson, D. Antonangeli, Thermal expansion of liquid Fe-S alloy at high pressure. *Earth and Planetary Science Letters* **563** (2021).

69. G. Morard, J. Siebert, D. Andrault, N. Guignot, G. Garbarino, F. Guyot, The Earth's core composition from high pressure density measurements of liquid iron alloys. *Earth Planet. Sci. Lett.* **373**, 169–178 (2013).

70. S. Kawaguchi, Y. Nakajima, K. Hirose, T. Komabayashi, H. Ozawa, S. Tateno, Y. Kuwagama, S. Tsutsui, A.Q.R. Baron, Sound velocity of liquid Fe–Ni–S at high pressure. *J. Geophys. Res. Solid Earth* **122**, 3624–3634 (2017).

71. K. Nishida, Y. Shibazaki, H. Terasaki, Y. Higo, A. Suzuki, F. Nobumasa, K. Hirose, Effect of sulfur on sound velocity of liquid iron under Martian core conditions. *Nat Commun* **11**, 1954 (2020).

72. G.H., Kaiura, J.M., Toguri, Densities of the molten FeS, FeS–Cu2S and Fe–S–O systems—utilizing a bottom-balance Archimedean technique. *Can. Metall. Quart.* **18**(2), 155-64 (1979).

73. M.W. Chase, NIST-JANAF Thermochemical Tables Fourth, J. Phys. Chem. Ref. Data Monograph **9** (1998).

74. Y. Shimoyama, H. Terasaki, S. Urakawa, Y. Takubo, S. Kuwabara, S. Kishimoto, T. Watanuki, A. Machida, Y. Katayama, T. Kondo, Thermoelastic properties of liquid Fe–C revealed by sound velocity and density measurements at high pressure. *J. Geophys. Res., Solid Earth* **121**(11), 7984–7995 (2016).

75. H. Terasaki, K. Nishida, Y. Shibazaki, T. Sakamaki, A. Suzuki, E. Ohtani, T. Kikegawa, Density measurement of Fe3C liquid using X-ray absorption image up to 10 GPa and effect of light elements on compressibility of liquid iron. *J. Geophys. Res.: Solid Earth* **115**, B06207 (2010).

76. G. Morard, Y. Nakajima, D. Andrault, D. Antonangeli, A. L. Auzende, E. Boulard, S. Cervera, A. N. Clark, O. T. Lord, J. Siebert, V. Svitlyk, G. Garbarino, M. Mezouar, Structure and Density of Fe-C Liquid Alloys Under High Pressure. *J. Geophys. Res. Solid Earth* **122**, 7813–7823 (2017).

77. A.-C. Plesa, S. Padovan, N. Tosi, D. Breuer. M. Grott, M. A. Wieczorek, T. Spohn, S. E. Smrekar, and W. B. Banerdt, The thermal state and interior structure of Mars, *Geophys. Res. Lett.* **45**, 12198-12209 (2018).

78. A. Khan, S. Ceylan, M. van Driel, D. Giardini, P. Lognonné, H. Samuel, Ni. C. Schmerr, S. C. Stähler, A. C. Duran, Q. Huang, D. Kim, A. Broquet, C. Charalambous, J. F. Clinton, P. M. Davis, M. Drilleau, F. Karakostas, V. Lekic, S. M. McLennan, R. R. Maguire, C. Michaut, M. P. Panning, W. T. Pike, B. Pinot, M. Plasman, J.-R. Scholz, R. Widmer-Schnidrig, T. Spohn, S. E. Smrekar, W. B. Banerdt, 2021, Upper mantle structure of Mars from InSight seismic data. *Science*. **373** (6553), 434-438 (2021).

79. M.A. Wieczorek, M. Meschede, SHTools: tools for working with spherical harmonics. *Geochem. Geophys. Geosyst.* **19**, 2574–2592 (2018).

80. D. Kim, V. Lekić, J. C. E. Irving, N. Schmerr, B. Knapmeyer-Endrun, R. Joshi, M. P. Panning, B. Tauzin, F. Karakostas, R. Maguire, Q. Huang, S. Ceylan, A. Khan, D. Giardini, M. A. Wieczorek, P. Lognonné, W. B. Banerdt. Improving constraints on planetary interiors with PPS receiver functions. *Journal of Geophysical Research: Planets*, **126**(11), e2021JE006983 (2021).

81. P.M. Mathews, T.A. Herring, B.A. Buffet, Modeling of nutation precession: new nutation series for non-rigid Earth, and insights into the Earth's interior. *J. Geophys. Res.* **107**, 2068 (2002).

82. B.A. Buffett, U.R. Christensen, Magnetic and viscous coupling at the core-mantle boundary: Inferences from observations of Earth's nutations. *Geophys. J. Int.* **171**, 143-152 (2007).

83. M Puica, V Dehant, M Folgueira, T Van Hoolst, and J Rekier. Analytical computation of total topographic torque at the core-mantle boundary and its impact on tidally driven length-of-day variations. *Geophysical Journal International*, **234**,585-596, 02 (2023).

84. W. Chen, WenBin Shen, New estimates of the inertia tensor and rotation of the triaxial nonrigid earth. *Journal of Geophysical Research: Solid Earth*, **115**(B12), (2010).

85. V.N. Zharkov, T.V. Gudkova, S.M. Molodensky, On models of Mars interior and amplitudes of forced nutations: 1. The effects of deviation of Mars from its equilibrium state on the flattening of the core-mantle boundary. *Phys. Earth Planet. Inter*. **172**(3), 324–334 (2009).

86. H. Moritz, Ed., *The Figure of the Earth: Theoretical Geodesy and the Earth's Interior* (Wichmann, Karlsruhe, 1990).

87. M. Greff-Lefftz, H. Legros, Some remarks about the degree-one deformation of the Earth, *Geophys. J. Int*., **131**, 699-723 (1997).

88. M. A. Richards, B. H. Hager, Geoid anomalies in a dynamic Earth, *J. Geophys. Res*. **89**, B7, 5987-6002 (1984).

89. P. Defraigne, V. Dehant, J. M. Wahr, Internal loading of an inhomogeneous compressible earth with phase boundaries, *Geophys. J. Int.* **125**, 173-192 (1996).

90. S. V. Panasyuk, B. H. Hager, A. M. Forte, Understanding the effects of mantle compressibility on geoid kernels, *Geophys. J. Int.* **124**, 121-133 (1996).

91. A. Broquet, M. A. Wieczorek, W. Fa, Flexure of the Lithosphere Beneath the North Polar Cap of Mars: Implications for Ice Composition and Heat Flow. *Geophys. Res. Lett.* **47**, e2019GL086746 (2020).

92. L.T. Elkins-Tanton, E.M. Parmentier, P.C. Hess, Magma ocean fractional crystallization and cumulate overturn in terrestrial planets: implications for Mars, Meteorit. *Planet. Sci.,* **38**, 1753-1771 (2003).

93. M.D. Ballmer, D.L. Lourenago, K. Hirose, R. Caracas, R. Nomura, Reconciling magma-ocean crystallization models with the present-day structure of the Earth's mantle. *Geochem Geophys Geosyst* **18**, 2785–2806 (2017).

94. C.-E. Boukaré, E.M. Parmentier, S.W. Parman, Timing of mantle overturn during magma ocean solidification, *Earth Planet. Sci. Lett*. **491**, 216-22 (2018).

95. M. Maurice, N. Tosi, H. Samuel, A.-C.Plesa, C. Hüttig, D. Breuer, Onset of solid-state mantle convection and mixing during magma ocean solidification. *J. Geophys. Res. Planets* **122**, 577–598 (2017).

96. H. Samuel, P. Lognonné, M. Panning, V. Lainey, The rheology and thermal history of Mars revealed by the orbital evolution of Phobos. *Nature* **569**, 523–527 (2019).

97. W.K. Hartmann, M. Malin, A. McEwen, M. Carr, L. Soderblom, P. Thomas, E. Danielson, P. James, J. Veverka, Evidence for recent volcanism on Mars from crater counts, *Nature* **397**, 586-590 (1999).

98. G. Neukum, R. Jaumann, H. Hoffmann, E. Hauber, J.W. Head, A.T. Basilevsky, T. McCord, Recent and episodic volcanic and glacial activity on Mars revealed by the High Resolution Stereo Camera. *Nature*, ***432***(7020), 971-979 (2004).

99. J. A. D. Connolly, The geodynamic equation of state: What and how. *Geochem. Geophys. Geosyst.* **10**, 10 (2009).

100. F. Nimmo, U.H. Faul, Dissipation at tidal and seismic frequencies in a melt-free, anhydrous Mars. *J. Geophys. Res*. **118**(12), 2558–2569 (2013).

101. A.M. Lejeune, P.Richet, Rheology of crystal-bearing silicate melts: an experimental study at high viscosities, *J. Geophys. Res*. **100**, 4215-4229 (1995).

102. D. Yamazaki, S. Karato, Some mineral physics constraints on the rheology and geothermal structure of earth's lower mantle, *Am. Mineralog*. **86**(4), 385-391 (2001).

103. M. Drilleau, H. Samuel, A. Rivoldini, M. Panning, P. Lognonné, Bayesian inversion of the Martian structure using geodynamic constraints. *Geophys. J. Int.* **226**, 1615–1644 (2021).

104. K. Lodders, B. Fegley, Jr An oxygen isotope model for the composition of Mars. *Icarus* **126**, 373–394 (1997).

105. G.J. Taylor, The bulk composition of Mars. *Chem. Erde* **73**(4), 401–420 (2013).

106. Y. Li, R. Dasgupta, K. Tsuno, B. Monteleone, N. Shimizu, Carbon and sulfur budget of the silicate Earth explained by accretion of differentiated planetary embryos. *Nat. Geosci.* **9**, 781–785 (2016).

107. G. Morard, S. Boccato, A.D. Rosa, S. Anzellini, F. Miozzi, L. Henry, G. Garbarino, M. Mezouar, M. Harmand, F. Guyot, E. Boulard, I. Kantor, T. Irifune, R. Torchio, Solving controversies on the iron phase diagram under high pressure. *Geophys. Res. Lett.* **45**, 11074-11082 (2018).

108. Y. Mori, H. Ozawa, K. Hirose, R. Sinmyo, S. Tateno, G. Morard, Y. Ohishi, Melting experiments on Fe-Fe3S system to 254 GPa. *Earth Planet. Sc. Lett.* **464**, 135-141 (2017).

109. Y. Fei, E. Brosh, Experimental study and thermodynamic calculations of phase relations in the Fe–C system at high pressure. *Earth Planet. Science Lett.* **408**, 155–162 (2014).

110. Y. Shibazaki, H. Terasaki, E. Ohtani, R. Tateyama, K. Nishida, K. Funakoshi, Y. Higo, High-pressure and high-temperature phase diagram for Fe0.9Ni0.1–H alloy. *Phys. Earth Planet. Inter.* **228** (2014), 192-201 (2014).